Alzheimer's Research & Therapy

RESEARCH

Open Access

Blockade of brain alkaline phosphatase efficiently reduces amyloid-β plaque burden and associated cognitive impairment

Lucia Soria-Tobar[1,2†], Laura Román-Valero[1†], Álvaro Sebastián-Serrano[2,3], Paloma Aivar[1], Beatriz Álvarez-Castelao[1,2] and Miguel Díaz-Hernández[1,2*]

Abstract

Background Alzheimer's disease (AD) is the most prevalent neurodegenerative disease. Three new drugs for AD based on monoclonal antibodies against the amyloid-β peptide (Aβ) have recently been approved because they favor the reduction of the burden of senile plaque in the AD patient's brain. Nonetheless, both drugs have very limited applicability and benefits and show several side effects. These limitations invite us to find alternative strategies for treating patients with AD. Here, we explored whether tissue-nonspecific alkaline phosphatase (TNAP), an ectoenzyme upregulated in the brain of AD patients and whose inhibition has beneficial effects on tau-induced pathology, is also efficient in reducing senile plaque burden.

Methods To evaluate whether TNAP may reduce cerebral senile plaque loading and Aβ-related toxicity, we use both pharmacological and genetic approaches. We analyze postmortem samples from human AD patients, APP/PS1 mice (a mouse model that mimics amyloid pathology observed in AD patients) treated or not with TNAP inhibitors, and the newly generated transgenic mouse line, TNAP-deficient APP/PS1 mice.

Results For the first time, we describe that genetic or pharmacological blockade of TNAP effectively reduces senile plaque burden by promoting its clearance, which leads to amelioration of cognitive impairment caused by Aβ-induced toxicity. These beneficial effects of TNAP inhibition occur concomitantly with higher microglial recruitment toward the senile plaque and increased microglial phagocytic capacity of Aβ by a mechanism involving metalloprotease-depending osteopontin processing. In addition, we also found that TNAP blockade favors LRP1-mediated transport of Aβ through the BBB.

Conclusions Here, we have shown that TNAP inhibition effectively reduces brain senile plaque burden and associated behavioral defects. Furthermore, given that we had previously reported that TNAP blockade also ameliorates Tau-induced neurotoxicity and increases lifespan of P301S tauopathy mouse model, we can state that TNAP blockade may be a novel and efficient therapy for treating patients with AD.

†Lucia Soria-Tobar and Laura Román-Valero contributed equally to this work.

*Correspondence:
Miguel Díaz-Hernández
migueldiaz@ucm.es

Full list of author information is available at the end of the article

Keywords Metalloprotease 9, Osteopontin, Low-density lipoprotein receptor-related protein 1, Tissue non-specific alkaline phosphate, Senile plaque

Background

Alzheimer's disease (AD) is a neurodegenerative disease characterized by the presence of two neuropathological hallmarks: intracellular neurofibrillary tangles assembled by hyperphosphorylated tau protein [1] and extracellular amyloid senile plaques primarily composed of the amyloid-β peptide (Aβ), which results from the sequential proteolysis of amyloid precursor protein (APP) by β- and γ-secretase [2]. Unfortunately, nowadays, there is no effective therapy for treating patients. Nevertheless, based on significant findings revealing that (i) less than 5% of AD cases are related to missense mutations or alternative splicing of APP and presenilin-1 and −2 (PS1 and PS2) genes, termed early-onset familial AD (FAD) [3, 4] and (ii) senile plaques emerge earlier than neurofibrillary tangles, even decades before the onset of the first symptoms [5, 6], many early efforts were aimed at developing therapeutic strategies favoring the reduction of the burden of senile plaques. Thus, several pre-clinical and clinical trials have been conducted to reduce cerebral Aβ peptide burden by (i) blocking or modulating β– and γ-secretases and/or enhancing the activity of a secretases [7, 8], (ii) preventing Aβ deposition in senile plaques using anti-aggregation agents [9], (iii) activating proteases that promote its degradation [10], vi) increasing the clearance of Aβ from the brain by lipoproteins [11] or v) enhancing the immune system by active or passive immunization [12, 13]. As a result of this last strategy, the FDA has recently approved three different drugs based on monoclonal antibodies against amyloid-β peptide, Lecanemab, Aducanumab, and Donanemab [14–16]. Nonetheless, these drugs have very limited applicability (only in middle cognitive impairment (MCI) patients), have several side effects, and their substantial cost burden raises questions about their cost-effectiveness [17, 18]. These limitations invite us to spend additional efforts on the research for alternative strategies to reduce cerebral Aβ peptide burden.

Recent studies have reported that AD patients present increased expression of one of the alkaline phosphatase isoforms in both brain and plasma, specifically tissue-nonspecific alkaline phosphatase (TNAP), which the *Alpl* gene, also known as *Akp2*, encodes for [19, 20]. This alteration was linked with a raised TNAP activity in the brain and plasma of AD patients, which points to TNAP as a novel plasma biomarker for MCI and AD [21]. Further studies also revealed that neural TNAP overexpression promotes intracellular Tau hyperphosphorylation and aggregation in neighboring neurons [22]. Conversely, genetic or pharmacological depletion of TNAP decreased neuronal hyperactivity, hippocampal neuronal death, and brain atrophy in the P301S mouse model mimicking tau pathology found in AD. Moreover, TNAP haploinsufficiency prevented anxiety-like behavior, motor deficiency, and increased memory capacity and life expectancy in these mice [20]. Furthermore, TNAP dephosphorylates a broad spectrum of substrates, including the extracellular nucleotides and the matricellular immunomodulatory cytokine Osteopontin (OPN). In particular, OPN, whose expression and phosphorylation status are regulated by TNAP [23], has recently been implicated in Aβ clearance and microglial activation [24]. Also, it has been reported that this ectoenzyme can also modulate purinergic receptors, including the P2X7 receptor (P2X7R) [25]. Interestingly, P2X7R inhibition reduces the senile plaque formation in a mouse model of FAD [26], rescues cognitive deficits, and improves synaptic plasticity in AD mice [27, 28]. In view of all these facts, we wonder if TNAP might also impact senile plaque formation and the Aβ related toxicity. To address this question, here, we evaluate how the genetic or pharmacological inactivation of TNAP impacts Aβ-related toxicity, using, for this purpose, a well-characterized FAD mouse model, the APP/PS1 mice [29].

Methods

Human brain tissues

Human samples were provided by the Banco de Tejidos Fundación CIEN (BT-CIEN, Madrid, Spain). A written informed consent for brain removal after death for diagnostic and research purposes was obtained from the brain donors and/or next of kin. Procedures, information, and consent forms were approved by the Bioethics Subcommittee of Fundación Cien Madrid, Spain (S19001). Frozen samples were obtained from the hippocampus of four patients with the clinical diagnosis of AD (three men aged 81, 76, and 86 years old and one woman aged 86 years) and four non-demented controls (three men aged 73, 83, and 74 years old and one woman aged 70 years). The postmortem delay in tissue processing was between 4 and 5 h in both groups.

Animals

All animal procedures were carried out at the Universidad Complutense de Madrid (UCM) in compliance with National and European regulations (RD1201/2005; 86/609/CEE) and following the International Council for the Laboratory Animal Science guidelines. The protocol for animal experiments was approved by the Committee of Animal Experiments at the UCM and

the Environmental Counselling of the Comunidad de Madrid, Spain (PROEX 185/17 and PROEX 137.8/22).

As previously described, TNAP null mice were generated by inactivating the mouse *Akp2* gene [30]. APP/PS1 mice were obtained from Jackson laboratory: [line B6;C3-Tg(APPswe, PSEN1dE9)85Dbo/Mmjax] stock number 034829. APP/PS1 are double transgenic mice expressing a chimeric mouse/human amyloid precursor protein (Mo/HuAPP695swe) and a mutant human presenilin 1 (PS1-dE9), both controlled by independent mouse prion protein (PrP) promoter and so directed to CNS neurons [29]. Double APP/PS1/TNAP$^{+/-}$ animals were generated by crossing heterozygote APP/PS1$^{+/-}$ and heterozygote TNAP$^{+/-}$ mice.

Animals were housed in a light and temperature-controlled humid environment, with a 12-hour light-dark cycle and a light onset at 08:00 a.m. The mice were grouped 4–6 per cage and allowed free access to water and food (ad libitum). All surgeries were performed under isoflurane anesthesia, and all efforts were made to minimize suffering. Investigators were blinded to the group allocation during the animal experiments.

We used 58 mice 9–11 months-old divided into the following groups; 20 wild-types (WT) mice, 11 females, and 9 males of; 20 APP/PS1$^{+/-}$ mice, 8 females, and 12 males; 8 TNAP$^{+/-}$, 3 females and 5 males; 10 APP/PS1/TNAP$^{+/-}$ mice, 4 females, and 6 males. When the animals were divided into different groups for whatever procedure, we kept the gender variable balanced among all groups.

PCR genotyping

According to the manufacturer's protocol, genomic DNA was obtained from tail biopsies using Wizard® SV Genomic DNA Purification System (Promega, Madison, WI, USA).

Simple PCR reactions were carried out using: for APP/PS1$^{+/-}$ mice Amplitools Master Mix (Biotools, Madrid, Spain), specific primers (150 nM each) and 2 µL of genomic DNA in a final volume of 12 µL; for TNAP$^{+/-}$ mice Amplitools Master Mix (Biotools, Madrid, Spain), specific primers (150 nM each) and 2 µL of genomic DNA in a final volume of 12 µL. Animals were genotyped using specific primers for APP Fw 5´-CCGAGATCTCT GAAGTGAAGATGGATG-3´ and Reverse 5´-CCTCTT TGTGACTATGTGGACTGATGTCGG-3´ and for PS1 FW 5´-CAGGTGGAGCAAGATG-3´ and Reverse 5´-GT GGATACCCCCTCCAGCCTAGACC; for TNAP Fw 5′-TGCTGCTCCACTCACGTCGAT-3′ and Reverse 5′-AG TCCGTGGGCATTGTGACTA-3′. PCR was carried out over 35 cycles: 94 °C for 45 s, 60 °C for 2 min, 72 °C for 2 min for APP/PS1$^{+/-}$ primers; over 40 cycles of 94 °C for 30 s, 58 °C for 1 min, and 72 °C for 5 min.

PCR amplification products were run on a 1.5% (w/v) agarose gel and stained with SYBR® Safe DNA Gel Stain (Life Technologies CA, USA). PCR bands were visualized by gel imaging system Gel Logic 200 Imaging System (Kodak, Rochester, NY, USA).

RNA extraction and quantitative real-time PCR (qRT-PCR)

Total RNA was extracted from hippocampi from human or adult mouse brains using a Speedtools Total RNA Extraction Kit (Biotools, Madrid, Spain) following the manufacturer's instructions. The animals were quickly sacrificed, in compliance with local laws, and the hippocampi were immediately dissected and frozen in dry ice to proceed with total RNA isolation. After digestion with TURBO DNase (Ambion), 1 µg of total RNA was reverse transcribed with 6 µg of random primers, 350 µM dNTPs, and M-MLV reverse transcriptase (all from Invitrogen, Madrid, Spain).

qRT-PCR reaction mixtures containing DNA Master SYBR Green I mix (Applied Biosystems, CA, USA) were incubated at 95 °C for 20 s followed by 40 PCR cycles (95 °C for 1 s and 60 °C for 20 s) in a StepOnePlus Real-Time PCR System (Applied Biosystems, CA, USA). The specific primers for mouse *P2rx7* Fw 5′- GGTGCCAGT GTGGAAATTG-3′ and Rv 5′- TAGGGATACTTGAAG CCACT-3′; for mouse gene encoding TNAP, *Alpl* (*Akp2)* Fw 5′- TGCCCTGAAACTCCAAAAGC-3′ and Rv 5′- T GTAGCTGGCCCTTAAGGATTC-3′; for *Il1b* Fw 5´- A AAGCTCTCCACCTCAATGG −3´ and Rv 5´- AGGCC ACAGGTATTTTGTCG −3´; for *Nlrp3* Fw 5´- TGCAA CCTCCAGAAACTGTG −3´and Rv 5´- AGAACCAAT GCGAGATCCTG-3´; for *Gapdh* Fw 5′-CACCACCAAC TGCTTAGCCC-3′ and Rv 5′-TGTGGTCATGAGCCCT TCC-3′ and for *Spp1* Fw 5´- AGCCTGCACCCAGATC CTATAG and Rv 5´-GCGCAAGGAGATTCTGCTTCT. Expression levels of mRNA were represented as $2^{-\Delta\Delta Ct}$, where the average cycle threshold (Ct) was obtained from triplicates of each sample. First, ΔCt means were normalized to parallel amplification of GAPDH as endogenous control. Next, ΔΔCt means were normalized to the average of corresponding controls.

Drug preparation and administration

Based on previous work studying the levamisole bioavailability after oral or intramuscular administration [31], this blood-brain barrier (BBB) permeable TNAP inhibitor was diluted at 23 mg/mL in vehicle solution as previously described [20]. The vehicle solution was calcium- and magnesium-free phosphate-buffered saline (PBS; 137 mM NaCl, 2.7 mM KCl, 5 mM Na_2HPO_4 $7H_2O$, 1.4 mM KH_2PO_4; pH 7.4) plus 0.2% DMSO (all reagents from Sigma; MS, USA). Following previous studies demonstrating that levamisole effectively reduces the cerebral TNAP activity in a tauopathies mouse model, P301S

mice [20], 12.5 µL of levamisole, corresponding to a dosage of 9.58 mg per kg of body weight, was daily intraperitoneally injected into 9–11 months-old APP/PS1$^{+/-}$ and WT mice for 20 days before beginning the behavioral assessment and it was maintained throughout the trials. The treatment protocol followed a single-blind design, by which the experimenter was blind for the genotype and treatment applied to each mouse (n=6–8 mice per group and condition).

Behavioral assay

All mice were handled for at least 3–4 consecutive days before testing. They were tested randomly, and the experimenter conducting the tests was blinded to the genotype/group. All behavioral devices were located in a sound-proof room, and the experimental area was homogeneously illuminated around 70 lx. All used devices were carefully cleaned with alcohol (70 ° proof) after each trial.

Open field test is an experimental test used to assay general locomotor activity levels, anxiety, and willingness to explore a novel environment. The apparatus consists of a transparent polycarbonate tank (42 cm × 42 cm). There is no need to habituate the mouse before the test. A single adult mouse was gently placed into the setup, and its position was video-tracked for 10 min. The analysis measured the amount of time spent by the mouse in the tank's center (17×17 cm) and the periphery (the surrounding area of the arena). The tendency to avoid the center of a novel environment and remain close to the wall of the tank is an index of anxiety. Data acquisition and analysis were performed automatically using Any-Maze software (Stoelting Co, Wood Dale, IL, USA).

Elevated plus maze test This test measures anxiety based on the animal's aversion to open spaces. The test uses an elevated, plus-shaped (+) apparatus with two open and two enclosed arms. There is no need to habituate the mouse before the test. A single adult mouse was gently placed into the center of the setup (at the intersection of the open and enclosed arms), and its position was video-tracked for 5 min. The analysis consisted of measuring the amount of time spent by the mouse in the different arms using Any-Maze software.

T-maze test The device was a symmetrical dark grey PVC T-shaped maze. The arms were 30 cm long, 9 cm wide, and 20 cm high and were connected at the center at a 90° angle to a 9 by 9 cm square. Both arms from the T could be blocked with a barrier. In the first part of this test, 1 of the two arms was blocked (alternated). The mouse was placed at the base of the leg of the T-maze. The mouse could freely explore the leg and the open arm of the T-maze for 5 min, after which the mouse was returned to its home cage. After 1 h, the blockage was removed from the T-maze, and the mouse was allowed to freely explore the leg and the old and novel arm of the T-maze for 5 min. Videos were analyzed using Any-Maze software. An automated setup was used to detect the mouse. In Any-Maze software, areas were assigned to the leg, the novel, and the old arm. When the center point of the mouse entered one of these areas, it was counted as an arm entry. The procedure is based on the natural tendency of rodents to prefer exploring a novel arm over a familiar one. During the task, the animal must remember which arm had been visited in the previous trial, making spontaneous alternation T-maze an optimal test for spatial working memory.

Barnes maze test *We adapted the shortened Barnes maze protocol described by Attar et al.* [32]. Briefly, The Barnes maze was a circular white PVC table with a diameter of 1 m elevated 1 m above the ground. In the periphery, there were 20 holes with a diameter of 5 cm at a regular interval. A rectangular black plastic box 16.2 cm long, 6.6 cm wide, and 8.5 cm high was attached underneath the maze and used as the escape chamber. The escape chamber contained a small staircase for the mice to climb down. The Barnes maze test consisted of 4 consecutive days covering 3 phases: day 0 habituation, days 1–3 training, and day 4 probe. For later analysis using Any-Maze software, all sessions were video-tracked. For the habituation phase, the mouse was placed in the center of the maze and allowed to explore the maze for 2 min freely. If the mouse did not enter the escape chamber within 1 min, it was gently guided toward the escape hole through a glass beaker. When the mouse entered the escape chamber, the escape hole was covered, and the mouse was left in the escape chamber for 2 min before returning the mouse to its individual cage.

In the training phase, mice were placed inside an opaque box in the center of the Barnes maze for 15 s. This allowed the mice to face a random direction when the cylinder was lifted, and the trial began. At the end of the holding period, the box was removed, and the mice were allowed to explore the maze for 2 min. If a mouse found the target hole and entered the escape cage during that time, the end-point of the trial, it was allowed to stay in the escape cage for 1 min before being returned to the holding cage. If it did not find the target hole, the mouse was guided to the escape hole using the glass beaker and allowed to enter the cage independently. The total number of trials used was 5. During the training phase, measures of primary latency (the time to identify the target hole the first time) were recorded.

On the probe day, 24 h after the last training day, the escape cage was removed. Mice were placed inside the opaque box in the center of the maze for 15 s before the

box was removed. Each mouse was given 2 min to explore the maze, and in the end, the mouse was returned to its holding cage. During the probe phase, we analyzed the time spent and the distance traveled to find the hole that previously contained the escape box.

Tissue processing for immunofluorescence and blood collection

Mouse brain Mice were deeply anesthetized using a mix of ketamine (200 mg/kg) and xylazine (12.5 mg/kg) diluted in PBS, administered as a single intraperitoneal injection. Anesthetized mice were perfused transcardially with cold PBS followed by cold PFA (pH 7.4) (all reagents from Sigma; MS, USA). Using the anesthesia explained above, blood samples were collected via cardiac puncture from the left ventricle using a 23–25 gauge needle (0.3–0.4 mL per mice). Blood was withdrawn slowly to prevent the heart from collapsing. Brains were dissected immediately and placed for 48 h in 4% PFA at 4 °C for post-fixation. Excess PFA was removed with three washes in PBS. Next, the fixed brains were placed in 30% sucrose in PBS for 48 h at 4 °C for cryoprotection. Samples were then embedded in OCT compound (Sakura, Finetek, Torrance, CA) and frozen using dry ice. Finally, 25-µm floating sections were cut in parasagittal or coronal planes with a cryostat (CM1950, Leica Microsystems, Wetzlar, Germany) and stored in a solution of 30% ethylene glycol, 30% glycerol and 0.1 M PBS at −20 °C until processed.

Human brain Whole brain from AD subjects was separate into two hemispheres, through a sagittal interhemispheric incision, and fixed in 10% buffered formalin for at least 3 weeks. Samples (2-mm-thick) of the hippocampus were then obtained through dissection, embedded in paraffin following standard protocols (Leica, HistoCore Pearl), and later sectioned (5 µm) by using a microtome (Microm HM 355 S) and stored at −80 °C until use.

Serum samples

Eppendorf tubes containing the whole blood samples were kept at 4°C until the formation of the blood clot which was removed by centrifugation at 1,000–1,500 x g for 10 min at 4°C. Following centrifugation, serum samples were immediately transferred into sterile polypropylene tubes 1.5 ml clearly labeled with the animal ID and date of collection.

Aβ ELISA

Human $A\beta_{1-40}$ amounts were determined by ELISA (Elabscience Biotech, Houston, USA) in the serum samples from APP/PS1$^{+/-}$, APP/PS1$^{+/-}$/TNAP$^{+/-}$ or levamisole treated APP/PS1$^{+/-}$ mice, according to the recommendations of the manufacturer. Serum samples from wild-type mice were used as the blank in the ELISA. Results were expressed in pg of human $A\beta_{1-40}$/ml of serum.

For immunofluorescence studies

For mouse Mouse slices were boiled in citrate buffer, washed in PBS, blocked for 1 h at room temperature (RT) with blocking solution (5% fetal bovine serum, 1% bovine serum albumin, 0.2% Triton-X100 in PBS) and then incubated at 37 °C for 1 h or overnight at 4 °C with primary antibodies diluted as follows: rabbit anti-TNAP (catalog GTX100817, Gentex, 1:500), mouse anti-GFAP (Merck, 1:200), rabbit anti-Iba-1 (catalog 019-19741, Wako, 1:100), mouse rat anti-CD68 (catalog 14-0681-82, Invitrogen, 1:100), mouse anti-Aβ (clone WO2, catalog MABN10, Merck, 1:500) in blocking solution. Subsequently, brain sections were washed with PBS buffer and incubated with secondary antibodies at the following dilutions: anti-rabbit IgG labelled with Alexa 555 (1:400), anti-rabbit IgG labelled with Alexa 488 (1:400), anti-mouse IgG labelled with Alexa 555 (1:400), anti-mouse IgG labelled with Alexa 488 (1:400), anti-rat IgG labelled with Alexa 647 (1:400) and 4′,6-diamidino-2-phenylindole (DAPI) staining (1:1,000). Finally, brain sections were washed with PBS and mounted in FluorSave (Calbiochem).

For Human Human sections were pre-incubated at 55 °C ON and then sequentially washed for 10 min in Xylene (catalog 131769.1611, Panreac, Barcelona, Spain), ethanol 100%, ethanol 96%, ethanol 70% and finally distilled H_2O in order to remove paraffin and rehydrated them. Later, the same protocols described for mouse samples were followed.

Image acquisition

Confocal images were acquired at RT with a TCS SPE microscope from Leica Microsystems equipped with a Plan Fluor 10× dry objective lens NA = 0.30, 40× Apochromat NA = 1.15 oil objective lens and 63× Apochromat NA = 1.3 oil objective lens (Leica Microsystems, Wetzlar, Germany) and 4 different lasers lines (405, 488, 565 and 647 nm). Photomicrographs were acquired using the Leica software LAS AF v2.2.1 software (Leica Microsystems, Wetzlar, Germany) and representative slices converted to TIFF files using ImageJ software.

Phagocytosis analysis

Brain sections containing the hippocampus were immunostained as described above. Rabbit polyclonal anti-Iba-1 (catalog 019-19741, Wako, 1:500), rat monoclonal antibody against the phagocytic marker CD68 (catalog 14-0681-82, Invitrogen, 1:100) and mouse anti-anti-Aβ (clone WO2, catalog MABN10, Merck, 1:500) were used. Subsequently, the sections were incubated with the corresponding fluorescent-labeled secondary antibodies

(Alexa 488, 594 or 647 from Thermofisher, Madrid, Spain). For each coverslip, at least 2 random photomicrographs of hippocampal senile plaques per animal were taken using the TCS SPE confocal microscope (Leica Microsystems, Wetzlar, Germany).

Phagocytosis of Aβ by microglia (Iba-1) was defined by the colocalization of APP with the lysosomal marker (CD68) within microglia surrounding amyloid plaques. Randomly photographed hippocampal senile plaques (containing an average of 6 to 18 microglial cells) were analyzed using FIJI software (ImageJ 1.53c, US National Institutes of Health, Bethesda, MD, United States). A mask with lysosomes was created based on CD68 channel. This mask was applied to the APP channel and only the events with a Mean Gray Value > 30 were considered positive for APP immunostaining. The percentage of lysosomes containing amyloid-β of the total microglial lysosomes (%CD68/APP) was represented.

Quantification of amyloid plaques, microglial recruitment inside amyloid plaque, and microglial migration

For each mouse (at least 8 mice per phenotype and treatment) 4 series (16 sections, 90 µm apart, approximately spanning from Bregma −0.95 mm to −3.78 mm according to [33] of Sect. (30 µm thick) were selected to be immunostained with antibodies anti-Iba-1 and/or anti-Aβ (clone WO2).

The number of amyloid plaques, positive to immunostaining with antibodies anti-Aβ, was counted for each series on blind-coded slides. Data are presented in box plots representing the distribution of the number of amyloid plaques per hippocampal section or cortical section per group (median, IQR, maximum, and minimum values). Confocal images of the whole-hippocampal area or including the primary somatosensory cortex and the lateral and medial parietal association cortex stained with antibody anti-Aβ (clone WO2) and Dapi (to identify and delimit hippocampal area) were acquired at low magnification to analyze the size of amyloid plaques. The background signal was determined by visual analysis, obtaining a range-value of cutoff 165–170 on a 0–255 scale with 0 = white and 255 = black. We measured the black areas generated on the images after a binary mask was applied over them. Data are presented in box plots representing the distribution of amyloid plaque size in μm^2 in the hippocampal area per group (median, IQR, maximum, and minimum values).

Microglial recruitment towards senile plaque was analyzed by adapting the method previously described by Martinez-Frailes et al. [34]. Briefly, the area around the senile plaque was subdivided into 3 regions or bins by drawing three concentrical circles from the center of the plaque of 40, 80, and 120 µm radius. The number of microglia cells was counted in each area or bin. Only the events positively stained with Iba-1 antibodies and with a higher area than 24.5 μm^2 were considered microglial cells.

Tissue processing for Western blot

Extracts for Western blot analysis were prepared by homogenizing fresh mouse hippocampi in ice-cold extraction buffer containing 20 mM Hepes, 100 mM NaCl, 50 mM NaF, 5 mM EDTA, 5 mM Na_3VO_4 (all reagents from Sigma; MS, USA), 1% Triton X-100, okadaic acid (Calbiochem), and Complete TM Protease Inhibitor Cocktail Tablets (Roche Diagnostics GmbH), pH 7.4. Samples were homogenized at 4 °C, and protein content was determined by Bradford assay. 20 µg of total lysates were run by SDS-PAGE on 10% Tris-Glycine-SDS gels and transferred to nitrocellulose membranes (Amersham Biosciences). The experiments were performed using the following primary antibodies: rabbit anti-P2X7R (catalog APR004, Alomone, 1:500), mouse anti-α-Tubulin (catalog T5168, Sigma-Aldrich, 1:10000), rabbit anti-IL-1β (catalog orb241007, Bionova, 1:200), mouse anti-total APP (clone 22C11 catalog MAB348, Merck, 1:5000); mouse anti-APP CTF (catalog A8717, Merck, 1:1000), rabbit anti-Nlrp3 (catalog NBP2-12446, Bio-techne, 1:200), rabbit anti-LRP1 (catalog 64099, Cell Signaling, 1:1000), and rabbit anti-MMP9 (catalog 13667, Cell Signaling, 1:1000), and rabbit anti-OPN (catalog AB63856, Abcam, 1:500). Next, membranes were washed for 10 min with PBS-Tween three times and incubated with secondary antibodies (1:10000) conjugated to fluorophores (emitting at 700–800 nm) for 1 h at room temperature. Protein bands were detected using the LI-COR Odyssey Classic and associated Image Pro analysis software (LI-COR Biosciences, Cambridge, UK). In the figures, we show the representative Western blot images fused for quantification with ImageJ software (v1.52n, NIH, Bethesda, MD, United States) are shown. In all cases, the average intensity value of the pixels in a background-selected region was calculated and was subtracted from each pixel in the samples. The densitometry values obtained in the linear range of detection with these antibodies were normalized with respect to the values obtained with an anti-α-tubulin antibody to correct for any deviation in loaded amounts of protein. Specifically, for OPN analysis, we used the same antibody that Rentsendorj et al. [35], which allows for the identification of two bands in 130 kDa and 66 kDa corresponding to the OPN full-length forms and two bands at 45 kDa and 32 kDa corresponding to the OPN cleaved fragments. In this case, graphs represent the ratio between the OPN-cleaved fragments and OPN full-length forms and the levels of OPN full-length forms normalized with respect to α-tubulin levels.

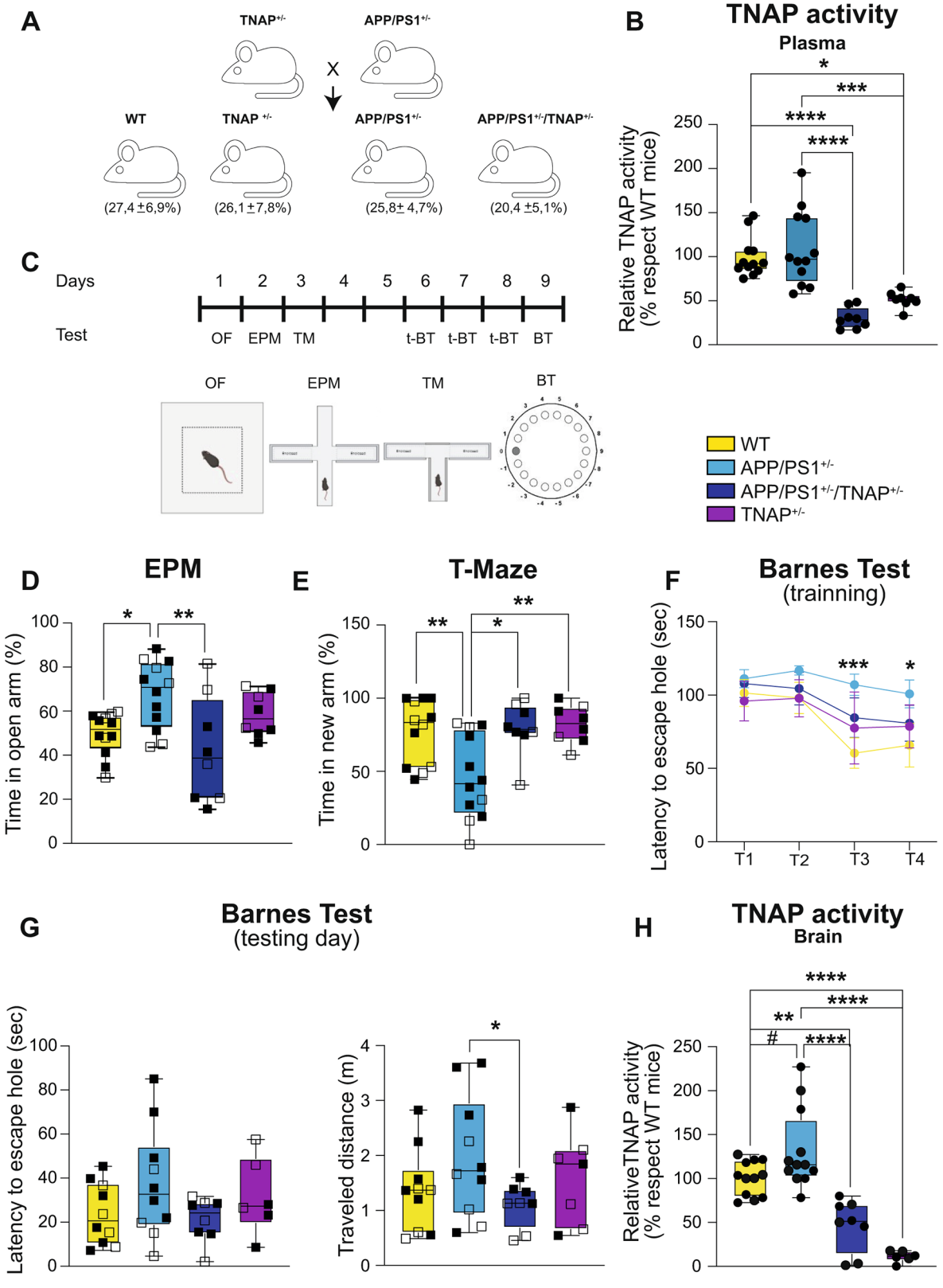

Fig. 1 (See legend on next page.)

(See figure on previous page.)

Fig. 1 TNAP haploinsufficiency prevents disinhibited behavior and improves spatial memory in APP/PS1$^{+/-}$ mice. (**A**) Breeding strategy: heterozygous TNAP mice (TNAP$^{+/-}$) were crossed with heterozygous APP/PS1 mice (APP/PS1$^{+/-}$) to obtain APP/PS1$^{+/-}$/TNAP$^{+/-}$ offspring. (**B**) TNAP activity in the plasma from WT ($n=12$), APP/PS1$^{+/-}$ ($n=12$), APP/PS1$^{+/-}$/TNAP$^{+/-}$ ($n=8$), and TNAP$^{+/-}$ ($n=8$) mice. Data are given as a percentage relative to WT mice, and the graphs show the distribution of values per group (median, IQR, maximum, and minimum values). (**C**) Timeline for Open Field (OF), Elevated Plus Maze (EPM), T-maze (TM), and Barnes Maze Test (BT or t-BT for training) behavioral assays performed by WT ($n=12$), APP/PS1$^{+/-}$ ($n=12$), APP/PS1$^{+/-}$/TNAP$^{+/-}$ ($n=8$), and TNAP$^{+/-}$ ($n=8$) groups. When indicated, black square data points represent males and open square data points represent females. (**D**) Percentage of time in open arms in the EPM. (**E**) Percentage of time in the new arm during the TM. (**F**) Latency to escape hole across the training sessions of the Barnes test. (**G**) Time spent (left graph) and distance traveled (right graph) to find the escape hole in BT test day. (**H**) TNAP activity in hippocampal homogenates from WT ($n=12$), APP/PS1$^{+/-}$ ($n=12$), APP/PS1$^{+/-}$/TNAP$^{+/-}$ ($n=8$)), and TNAP$^{+/-}$ ($n=8$) mice. Data are given as a percentage relative to WT mice, and the graphs show the distribution of values per group (median, IQR, maximum, and minimum values). $^{\#}P \leq 0.08$; * $P \leq 0.05$; ** $P \leq 0.01$ or **** $P \leq 0.0001$; using a one-way ANOVA followed by Tukey's post hoc test

TNAP activity

Serum samples 10 µL were brought to 0.2 mL with the following reaction conditions: 0.2 M Diethanolamine and 1 mM $MgCl_2$ (Merck Life Science S.L.U, Madrid, Spain), pH 9.8, incubated with 4 mM p-nitrophenyl phosphate (Merck Life Science S.L.U, Madrid, Spain) at 37 °C with agitation. All samples were assayed in duplicate. The background signal was determined by pre-incubating plasma samples with 150 µM levamisole for 5 min, 37 °C, before adding 4 mM p-nitrophenyl phosphate in the presence of levamisole. Samples absorbance was measured at 405 nm, 25 °C, in a spectrophotometer.

Mouse brain samples A portion of hippocampal tissue was homogenized with a Teflon glass homogenizer in 10 mm Tris-HCl buffer, pH 8.0, supplemented with 0.25 M sucrose and protease inhibitor mixture (EDTA-free CompleteTM, Roche Diagnostics) or with a protease inhibitor mixture containing 1 mm PMSF, 10 µg/mL aprotinin, 10 µg/mL leupeptin, and 50 µg/mL pepstatin. Aliquots from homogenates were assayed at 25 °C in the following reaction mix: 0.2 M diethanolamine buffer, pH 9.8, 1 mM $MgCl_2$, and 5 mM p-nitrophenyl phosphate in the presence or in the absence of 5 mM levamisole (all reagents from Sigma; MS, USA). Reactions were stopped after 20 min with 0.1 M NaOH. Protein concentrations were quantified by Bradford assay. TNAP activity was determined as the absorbance of the liberated p-nitrophenol at 405 nm and normalized to cellular protein content.

Statistics

Data in box plots represent the distribution of numeric data value per group (median, IQR, maximum, and minimum values). The numbers of mice per group used in each experiment are annotated as "n" in the corresponding figure legends. Figures and statistical analyses were generated using GraphPad Prism (v10.00, www.graphpad.com). To assess whether the data met the normal distribution, the Shapiro-Wilk or Kolmogorov-Smirnov tests were used. The ROUT method was used to identify outlier values. For two-group comparison; data were analyzed with a two-tailed unpaired Student's t-test. For multiple comparisons, when only one variable was compared, data were analyzed by one-way ANOVA followed by Tukey's post hoc test. The statistical test used, and *p*-values are indicated in each figure legend. Significance was considered at $^{*}P \leqq 0.05$ throughout the study. Marginal significance was considered at $\# P \leqq 0.08$.

Results

Partial *Akp2* gene silencing ameliorates cognitive decline in APP/PS1 $^{+/-}$ mice, a FAD mice model

To elucidate if TNAP plays a crucial role in Aβ peptide-induced toxicity, we generated a new transgenic mouse model by crossbreeding the well-characterized amyloid mice model of FAD (APP/PS1$^{+/-}$) and TNAP-deficient mice (Fig. 1A). Since homozygous *Akp2* null mice die before weaning [30], we crossed APP/PS1$^{+/-}$ mice with the heterozygous *Akp2* deficient animals (TNAP$^{+/-}$). No perinatal death was observed. Almost half of the generated offspring mice were haploinsufficient for *Akp2* (46.5%). While 20.4% of total offspring expressed the mutant APP and mutant PSEN1 in combination with heterozygote deficiency of TNAP (APP/PS1$^{+/-}$/TNAP$^{+/-}$ mice; Fig. 1A). As expected, both TNAP$^{+/-}$ and APP/PS1$^{+/-}$/TNAP$^{+/-}$ mice showed a significantly lower plasmatic TNAP activity compared to both the WT and the APP/PS1$^{+/-}$ mice (Fig. 1B). The TNAP activity mean±s.e.m values were 109.0±12,2% for the APP/PS1$^{+/-}$ group; 29.9±4.2% for the APP/PS1$^{+/-}$/TNAP$^{+/-}$ group and 51.1±3.2% for the TNAP$^{+/-}$ group, all relative to the TNAP activity in the WT mice. Because previous studies reported that APP/PS1$^{+/-}$ mice show a cognitive decline and impaired spatial memory in adulthood [36–38], we analyzed the behavior of mice from all generated genotypes at the age of 9–11 months (Fig. 1C). To evaluate the anxiety/disinhibition profile, mice were assessed by elevated plus maze (EPM) and Open field (OF) tests. Our analysis showed that APP/PS1$^{+/-}$ mice spent more time exploring the open arms in the EPM than their WT littermates, suggesting a decreased anxious behavior or an increase in the disinhibitory phenotype (Fig. 1D). Interestingly, APP/PS1$^{+/-}$/TNAP$^{+/-}$ mice spent less time in open arms than APP/PS1$^{+/-}$ mice, suggesting that partial TNAP silencing protects against the disinhibitory phenotype exhibited by APP/PS1$^{+/-}$ mice (Fig. 1D).

As reported in previous studies [39], OF test failed to clearly detect an increased disinhibitory phenotype in APP/PS1$^{+/-}$ mice, as observed in the EPM (Supplementary Fig. 1A). Only a marginally significant increase in the number of entries in the APP/PS1$^{+/-}$ mice was detected compared to WT mice. However, it did reveal that APP/PS1$^{+/-}$/TNAP$^{+/-}$ mice entered the central area fewer times than APP/PS1$^{+/-}$ mice in the OF test, despite both groups traveling a similar distance (Supplementary Fig. 1A). Together, our results point out that genetic depletion of TNAP leads to a reduction in anxiety-like behavior. Next, to evaluate the spatial memory capacity, mice were subjected to the T-maze and Barnes maze tests (Fig. 1C). In the T-maze, APP/PS1$^{+/-}$ mice spent less time exploring the new arm than WT mice, suggesting impaired short-term spatial memory (Fig. 1E). In agreement with this hypothesis, APP/PS1$^{+/-}$ mice took longer to find the escape hole during the Barnes test training sessions than WT mice (Fig. 1F). Notably, APP/PS1$^{+/-}$/TNAP$^{+/-}$ mice spent similar time to WT mice and less time than APP/PS1$^{+/-}$ mice to explore the new arm in T-maze or find the escape hole during the training sessions of the Barnes test (Fig. 1E-F). Curiously, although APP/PS1$^{+/-}$/TNAP$^{+/-}$ mice only tended to take less time to find the escape hole, they traveled a less distance than APP/PS1$^{+/-}$ mice on the Barnes test day (Fig. 1G). These results suggest that a reduced *Akp2* genetic loading also protects against the spatial memory impairment developed by APP/PS1$^{+/-}$ mice. It is to be noted that TNAP$^{+/-}$ mice do not show significant differences compared with WT mice in any assessed behavioral tests (Fig. 1D-H). Finally, no significant differences were found between the sexes when behavioral tests were analyzed considering this condition (Fig. 1D-H).

TNAP hemizygosity reduces the development of amyloid plaques in vivo without affecting the APP processing

After the behavioral assessment, mice were sacrificed and analyzed to evaluate the impact of partial *Akp2* gene silencing on Aβ peptide-induced toxicity. Initially, we measured TNAP activity in the brains. Similar to what was observed in plasma, TNAP$^{+/-}$ and APP/PS1$^{+/-}$/TNAP$^{+/-}$ mice presented a significantly lower brain TNAP activity than WT (11.2±2.6% and 46.6±10.5% of TNAP activity relative to WT mice, respectively, data correspond to the mean±s.e.m.; Fig. 1H) or than APP/PS1$^{+/-}$ mice, which showed 132.0±13.7% of TNAP activity detected in WT mice (data correspond to the mean±s.e.m.; Fig. 1H). Interestingly, APP/PS1$^{+/-}$ mice showed a slight increase in brain enzymatic activity compared to WT mice. This increase was marginally statistically significant when all groups were compared but reached statistical significance when compared only with WT mice (Fig. 1H). As expected, in the APP/PS1$^{+/-}$/TNAP$^{+/-}$ mice, the reduction in enzymatic activity coincided with the reduction in TNAP mRNA levels (Supplementary Fig. 1B).

Once we verified that our experimental approach effectively reduced TNAP activity in the brain, we assessed whether this reduction affected the amyloid plaque burden in the hippocampus of APP/PS1$^{+/-}$ mice. Immunohistological studies using selective markers against Aβ (WO2) revealed that APP/PS1$^{+/-}$/TNAP$^{+/-}$ mice present a clear reduction in the number and size of hippocampal senile plaques compared to APP/PS1$^{+/-}$ mice (Fig. 2A-C). Similar results were obtained in the primary somatosensory cortex and the lateral and medial parietal association cortex from a sub-cohort of APP/PS1$^{+/-}$ and APP/PS1$^{+/-}$/TNAP$^{+/-}$ mice (supplementary Fig. 1C-E). It is to be noted that non-significant changes were associated with mice sex. Initially, we evaluated whether the observed effects were due to TNAP modulating of the amyloidogenic APP processing. To this end, we measured the products of both α- and β-secretase in the hippocampus of APP/PS1$^{+/-}$ and APP/PS1$^{+/-}$/TNAP$^{+/-}$ mice, which are involved in the non-amyloidogenic and amyloidogenic APP processing (C83 and C99 fragments, respectively). In this study, we used an antibody that recognizes the C-terminal region of APP. Our results revealed that partial inactivation of cerebral TNAP did not affect α- or β-secretase activities in APP/PS1$^{+/-}$ mice (Fig. 2D-G), nor the APP protein levels (Fig. 2D and H).

TNAP deficiency impacts microglial functionality, helping to reduce the burden of senile plaques

Given that senile plaques induce a persistent activation of microglia cells [40], driving phagocytosis and plaque degradation, we decided to analyze whether TNAP deficiency impacts microglial functionality and, thus, contributes to the reduction in senile plaque burden observed in the APP/PS1$^{+/-}$/TNAP$^{+/-}$ mice. Initial immunohistological studies using selective TNAP antibodies and the microglial marker Iba-1 revealed that Iba-1-positive microglial cells from APP/PS1$^{+/-}$ mice exhibited scattered punctuated labeling for TNAP (Fig. 2I). Further studies using WO2 antibody to identify senile plaques revealed that similar punctate labeling for TNAP occurred in the hippocampal area covered by the senile plaques (Fig. 2J). Notably, similar punctuated staining for TNAP was observed within senile plaques detected in postmortem hippocampal slices from human AD patients (Fig. 2K). Next, to elucidate how TNAP affects microglial cells, several functions, such as microglial phagocytic, migratory, and secretory capacities, were analyzed in both APP/PS1$^{+/-}$ and APP/PS1$^{+/-}$/TNAP$^{+/-}$ mice. Using immunofluorescence studies, we found a higher microglial density inside the plaques of APP/PS1$^{+/-}$/TNAP$^{+/-}$ mice than in the plaques of APP/

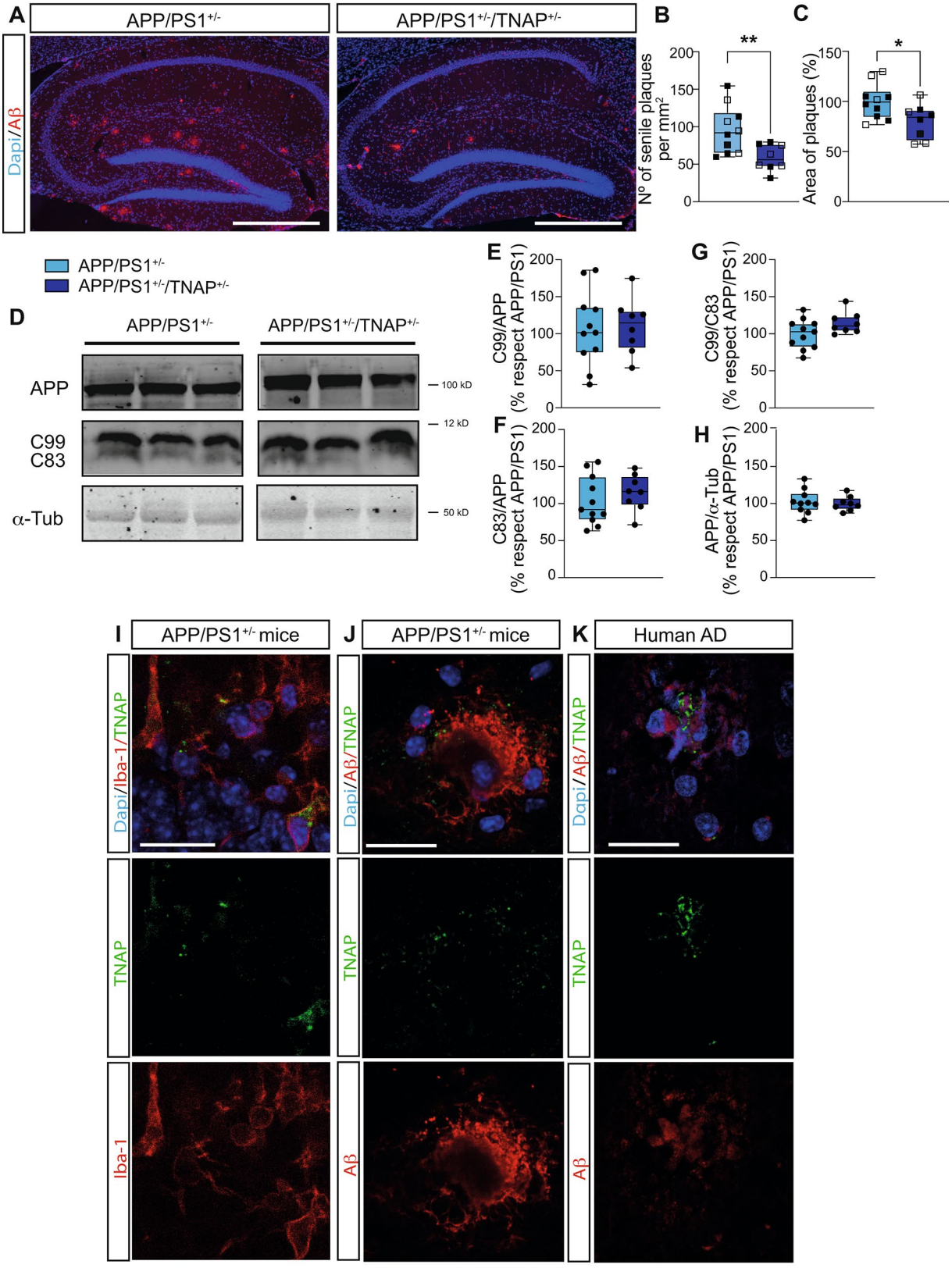

Fig. 2 (See legend on next page.)

(See figure on previous page.)

Fig. 2 TNAP haploinsufficiency prevents the development of amyloid plaques in APP/PS1$^{+/-}$ mice. (**A**) Representative confocal microscopy images of senile plaques (APP red channel) in the hippocampus of APP/PS1$^{+/-}$ and APP/PS1$^{+/-}$/TNAP$^{+/-}$ mice. Nuclei were stained with DAPI. Scale bar: 500 µm. (**B**, **C**) Graphs represent the distribution of values per group (median, IQR, maximum, and minimum values) of the number (**B**) and the percentage of area (**C**) of hippocampal senile plaques. When indicated, black square data points represent males and open square data points represent females. (**D**) Representative immunoblot of APP and fragments C99 and C83 in homogenates from the hippocampus of APP/PS1$^{+/-}$ and APP/PS1$^{+/-}$/TNAP$^{+/-}$ mice. (**E-H**) Quantification of C99/APP (**E**), C83/APP (**F**), C99/C83 (**G**), and APP (**H**) protein levels in the hippocampus of APP/PS1$^{+/-}$ ($n = 10$ or 11) and APP/PS1$^{+/-}$/TNAP$^{+/-}$ ($n = 8$) mice. Levels of α-tubulin were used as loading control for normalization purposes. Data are given as a percentage relative to APP/PS1$^{+/-}$ mice, and graphs show the distribution of values per group (median, IQR, maximum, and minimum values). **I-K.** Representative confocal microscopy images showing TNAP punctate pattern (green channel) in senile plaques (WO2, red channel) (**I**) and TNAP in microglial cells (Iba-1, green channel) (**J**), both in the hippocampus of APP/PS1$^{+/-}$ mice. Samples from Alzheimer´s disease patients mimic the TNAP punctate pattern (green channel) in hippocampal senile plaques (WO2, red channel) (**K**) Nuclei were stained with DAPI. Scale bar: 20 µm. Data in box plots represent median ± SD. * $P \leq 0.05$ or ** $P \leq 0.01$; using an unpaired two-tailed Student's *t*-test

PS1$^{+/-}$ mice (Fig. 3A-B). Furthermore, when we analyzed microglial recruitment, we observed that APP/PS1$^{+/-}$/TNAP$^{+/-}$ mice had more microglial cells in the vicinity of the senile plaque and fewer in locations further away from the plaque than APP/PS1$^{+/-}$ mice (Fig. 3A and C). These results suggest that cerebral TNAP deficiency promotes the microglia's recruitment toward the senile plaque.

Next, to determine the involvement of recruited microglia in the clearance of senile plaques, microglial phagocytosis was evaluated by immunostaining with antibodies anti-Aβ, Iba1, and the phagocytic marker CD68. Our analysis showed that hippocampal microglial cells from APP/PS1$^{+/-}$/TNAP$^{+/-}$ mice have more CD68-positive-phagocytic microvesicles phagocytosing Aβ than those from APP/PS1$^{+/-}$ mice (18.1 ± 4.3% of phagocytic microvesicles are phagocytosing Aβ peptides in APP/PS1$^{+/-}$ mice versus 53.8 ± 6.9% in APP/PS1$^{+/-}$/TNAP$^{+/-}$ mice, data correspond to the mean ± s.e.m.; Fig. 3D-E).

To evaluate the microglial secretion, considering the close relationship between TNAP and P2X7R [25], we focused on analyzing whether TNAP deficiency may affect the P2X7R/NLRP3/IL1β axis in the hippocampus. Our analysis revealed that TNAP deficiency reverted the increased levels of NRLP3 and P2X7R detected in APP/PS1$^{+/-}$ mice (Fig. 3F-H). However, we did not observe a reduction of IL1β levels in APP/PS1$^{+/-}$/TNAP$^{+/-}$ mice (Fig. 3F and I). Similar results were obtained when analyzing the mRNA levels of *Nrlp3*, *P2rx7*, and *Il1b* mRNA levels in APP/PS1$^{+/-}$ and APP/PS1$^{+/-}$/TNAP$^{+/-}$ mice (Supplementary Fig. 2A-C). No significant changes were observed in NLRP or IL1β expression levels between WT or TNAP$^{+/-}$ mice (supplementary Fig. 2E-G). Altogether, our findings support that cerebral TNAP deficiency promotes microglial recruitment toward senile plaques and the subsequent senile plaque phagocytosis, which may be contributing to a reduction in the number and size of senile plaques observed in APP/PS1$^{+/-}$/TNAP$^{+/-}$ mice.

Next, we evaluate the possible involvement of OPN in the reduction of senile plaques burden observed in APP/PS1$^{+/-}$/TNAP$^{+/-}$ mice. OPN protein levels were analyzed using a well-characterized polyclonal antibody recognizing the full length and its polymeric forms as well as its MMP-cleaved fragments, including the anti-inflammatory 32 kD C-terminus fragment [41–43] (Fig. 3J). Interestingly, our results show that APP/PS1$^{+/-}$/TNAP$^{+/-}$ mice present a higher percentage of cleaved-OPN than WT mice or APP/PS1$^{+/-}$ mice (Fig. 3J-K). Similar results were observed when comparing TNAP$^{+/-}$ and WT mice (supplementary Fig. 2E and 2 H). Moreover, we found that APP/PS1$^{+/-}$/TNAP$^{+/-}$ mice exhibited a significant increase in the total OPN protein levels (Fig. 3J and L) as well as in messenger RNA levels (*Spp1* mRNA) compared with WT mice (Supplementary Fig. 2D). However, non-significant changes in OPN expression levels were observed when comparing TNAP$^{+/-}$ and WT mice (supplementary Fig. 2E and 2I).

TNAP deficiency promotes senile plaque clearance by favoring Aβ transport across the blood-brain barrier and upregulating the proteases involved in its degradation

Lipoproteins may increase the clearance of Aβ from the brain [11], by promoting the amyloid transport from the brain to peripheral blood [44]. Considering that the low-density lipoprotein receptor-related protein 1 (LRP1) modulates the cellular uptake, trafficking, degradation, and/or aggregation of Aβ peptides [45], we evaluate whether the TNAP deficiency may be affecting LRP1. As previously described [46], we found that APP/PS1$^{+/-}$ mice present significantly lower LRP1 levels than WT mice. However, APP/PS1$^{+/-}$/TNAP$^{+/-}$ mice did not show this reduction and presented similar LRP1 levels than WT mice (Fig. 3M-N). However, no significant changes in LRP1 expression levels between WT or TNAP$^{+/-}$ mice were observed (supplementary Fig. 2E and 2 J). Based on previous work reporting that $A\beta_{1-40}$ binds to LRP1 with higher affinity than $A\beta_{1-42}$ [47], we wondered if TNAP-induced increased LRP1 expression also impacts $A\beta_{1-40}$ transport through the BBB. Notably, when we measured the human $A\beta_{1-40}$ levels in mouse serum, we found that APP/PS1$^{+/-}$/TNAP$^{+/-}$ mice have higher blood levels of human $A\beta_{1-40}$ levels than the APP/PS1$^{+/-}$ mice (Fig. 3O). These findings suggest that increased levels of LRP1 in

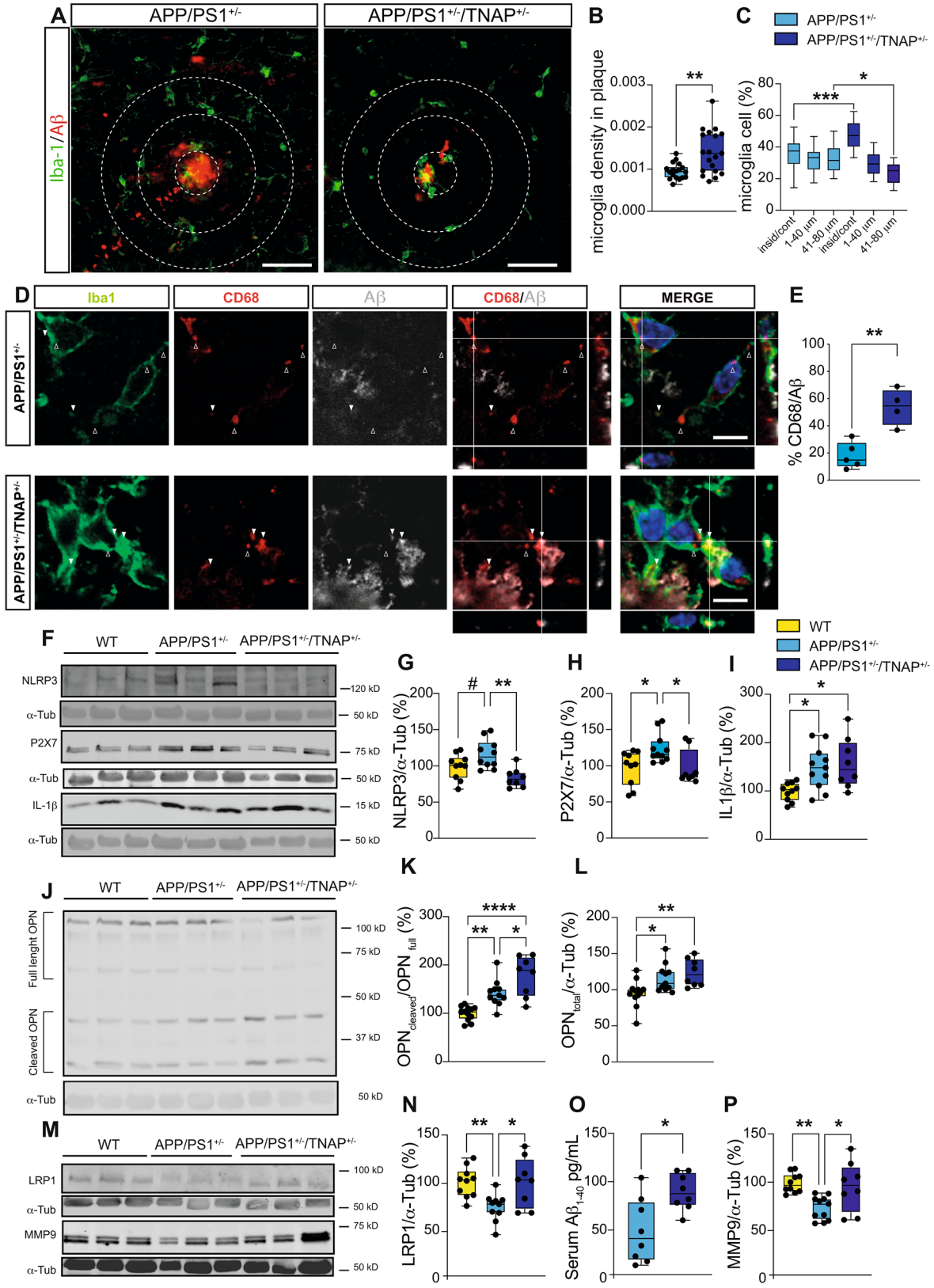

Fig. 3 (See legend on next page.)

(See figure on previous page.)

Fig. 3 TNAP hemizygosity influences microglial response in APP/PS1$^{+/-}$ mice. (**A**) Representative immunofluorescence images of hippocampal sections stained with the microglial marker Iba-1 (green channel) used to assess microglial density in the vicinity of senile plaques (WO2, red channel) in APP/PS1$^{+/-}$ and APP/PS1$^{+/-}$/TNAP$^{+/-}$ mice. Distances of 40 and 80 µm from the periphery of senile plaques are identified with white dashed lines. Scale bar: 50 µm. (**B**, **C**) The graphs represent the distribution of values per group (median, IQR, maximum, and minimum values) of the density of hippocampal microglia per plaque area (µm^2) (**B**) and the percentage of microglia cells found in every delimitated area (**C**) (n ≧ five mice per genotype). ** $P \leq 0.01$; using an unpaired two-tailed Student's *t*-test or * $P \leq 0.05$ or *** $P \leq 0.001$; using a one-way ANOVA followed by Tukey's post hoc test (**D**) Representative single confocal microscopy and orthogonal views showing CD68 positive-phagocytic microvesicles (red channel) phagocytosing Aβ peptides (Aβ, grey channel) within microglia (Iba-1, green channel) surrounding hippocampal senile plaques. (**E**) Graph represents the distribution of values per group (median, IQR, maximum, and minimum values) of the percentage of lysosomes containing amyloid-β of the total microglial lysosomes. ** $P \leq 0.01$; using an unpaired two-tailed Student's *t*-test (**F**) Representative immunoblot of NLRP3, P2X7, and IL-1β in homogenates from the hippocampus of WT, APP/PS1$^{+/-}$ and APP/PS1$^{+/-}$/TNAP$^{+/-}$ mice. (**G-I**) Quantification of NLRP3 (**G**), P2X7 (**H**), and IL-1β (**I**) protein levels in the hippocampus of WT ($n = 10$), APP/PS1$^{+/-}$ ($n = 10$ or 11), and APP/PS1$^{+/-}$/TNAP$^{+/-}$ ($n = 8$) mice. (**J**) Representative immunoblot using an antibody recognizing cleaved and full-length OPN in homogenates from the hippocampus of WT, APP/PS1$^{+/-}$ and APP/PS1$^{+/-}$/TNAP$^{+/-}$ mice. (**K** and **I**) Quantification of the ratio between cleaved OPN and full-length OPN (**K**) and total OPN (**L**) protein levels in the hippocampus of WT ($n = 11$), APP/PS1$^{+/-}$ ($n = 11$), and APP/PS1$^{+/-}$/TNAP$^{+/-}$ ($n = 8$) mice. (**M**) Representative immunoblot of LRP1 and MMP9 in homogenates from the hippocampus of WT, APP/PS1$^{+/-}$ and APP/PS1$^{+/-}$/TNAP$^{+/-}$ mice. Quantification of LRP1 (**M**) and MMP9 (**P**) protein levels in the hippocampus of WT ($n = 10$), APP/PS1$^{+/-}$ ($n = 10$ or 12), and APP/PS1$^{+/-}$/TNAP$^{+/-}$ ($n = 8$) mice. Levels of α-tubulin were used as loading control for normalization purposes. Data are given as a percentage relative to WT mice, and graphs show the distribution of values per group (median, IQR, maximum, and minimum values). $^{\#}P \leq 0{,}08$; * $P \leq 0.05$ or ** $P \leq 0.01$; using a one-way ANOVA followed by Tukey's post hoc test. **O.** $A\beta_{1-40}$ levels in serum samples from APP/PS1$^{+/-}$ ($n = 8$) and APP/PS1$^{+/-}$/TNAP$^{+/-}$ ($n = 8$) mice. Serum samples were analyzed via $A\beta_{1-40}$-detecting ELISA. * $P \leq 0.05$, using an unpaired two-tailed Student's *t*-test

APP/PS1$^{+/-}$/TNAP$^{+/-}$ mice contributes to improving the Aβ transport across the BBB.

Finally, given that matrix metalloproteinase-9 (MMP9) is involved in the proteolytic cleaved of OPN [41, 43] and is also able to degrade Aβ fibrils from the senile plaques [48], we decided to study if this enzyme is affected by a deficient TNAP loading. Our analysis revealed that APP/PS1$^{+/-}$ mice present a significant reduction in MMP9 levels compared with WT mice. However, this decrease was non-observed in APP/PS1$^{+/-}$/TNAP$^{+/-}$ mice, which exhibited similar MMP9 levels to WT mice (Fig. 3M and P). No significant changes were observed in MMP9 expression levels between WT or TNAP$^{+/-}$ mice (supplementary Fig. 2E and K).

In vivo pharmacological TNAP inhibition prevents cognitive decline and reduces the burden of senile plaques in APP/PS1$^{+/-}$ mice

Once the beneficial effects of TNAP haploinsufficiency on an AD amyloidosis mouse model were demonstrated, we tested whether pharmacological inhibition of this enzyme reproduced these benefits in vivo. To this end, a new set of APP/PS1$^{+/-}$ and WT mice were treated daily with levamisole (9.3 mg/kg, intraperitoneally) or vehicle solution for 20 days before being evaluated by a battery of behavioral tests similar to that used in the genetic approach (Fig. 4A). After behavioral tests, mice were sacrificed and analyzed. The capacity of levamisole to block TNAP was determined by measuring cerebral and plasma enzymatic activity. At the brain level, a significant reduction of TNAP activity was detected in levamisole-treated mice compared with untreated counterparts (levamisole-treated WT and levamisole-treated APP/PS1$^{+/-}$ mice showed 63.3 ± 15.5% and 43.2 ± 13.6% reduction of TNAP activity compared to WT mice, respectively, data correspond to the mean ± s.e.m.; Fig. 4B, left panel). Of note, while pharmacological inhibition of TNAP did not significantly reduce TNAP mRNA levels in the brain of WT mice, this approach induced a significant reduction of TNAP mRNA levels in the brain of APP/PS1$^{+/-}$ mice (Supplementary Fig. 3A). Similar results were observed for plasma TNAP activity (levamisole-treated WT and levamisole-treated APP/PS1$^{+/-}$ mice showed 43.7 ± 14.6% and 47,1 ± 8.2% reduction of TNAP activity compared to WT mice, respectively, data correspond to the mean ± s.e.m.; Fig. 4B, right panel).

Interestingly, although pharmacological TNAP blockage effectively reduces TNAP activity in the blood and brain, very limited beneficial effects were observed in the behavioral tests (Fig. 4C-F). So, and agree with gene silencing results, pharmacological blockade of TNAP avoids APP/PS1$^{+/-}$ mice spending significantly more time in open arms than WT treated or not with levamisole in the EPM test (Fig. 4C). However, no beneficial effects were observed in the OF test (supplementary Fig. 3B). It is to be noticed that similarly observed in the genetic approach, levamisole-treated APP/PS1$^{+/-}$ mice took a similar time to WT but less than APP/PS1$^{+/-}$ mice to find the escape hole in Barnes test´s training sessions (Fig. 4D). As was observed in the genetic approach, these beneficial effects were not obvious on the test day (Fig. 4E). Unexpectedly, pharmacological TNAP inhibition did not prevent APP/PS1$^{+/-}$ mice from spending less time exploring the new arm than WT mice in the T-maze test (Fig. 4F). Similar to the genetic approach, no significant sex-related differences were found on behavioral tests (Fig. 4B-F).

After behavioral assessment, mice were biochemically analyzed. Results showed that pharmacological inhibition of TNAP reduces the number but not the size of senile plaques in the hippocampus of APP/PS1$^{+/-}$ mice (Fig. 4G-I). Similar results were obtained in the cortical

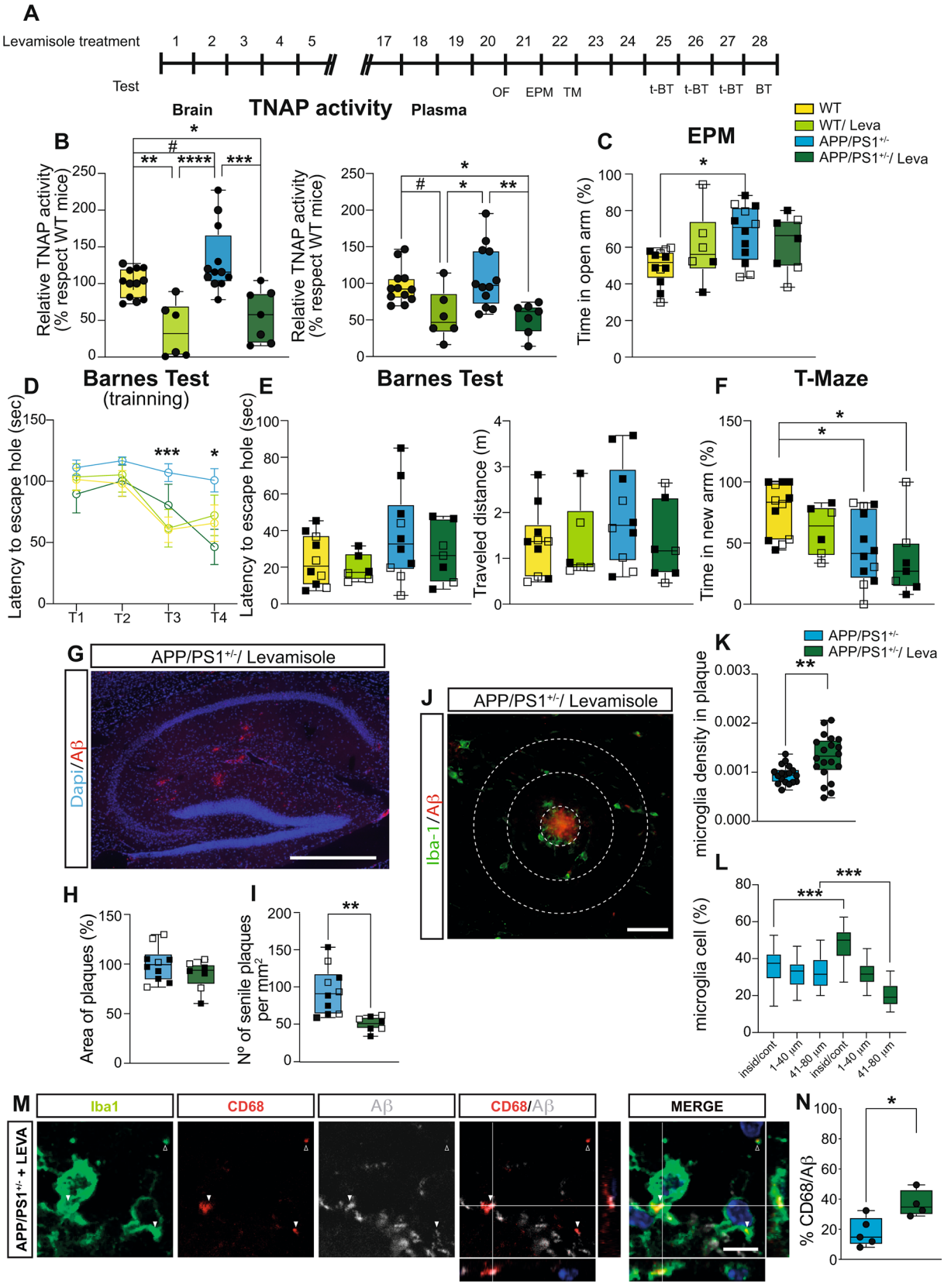

Fig. 4 (See legend on next page.)

(See figure on previous page.)

Fig. 4 TNAP pharmacological inhibition prevents cognitive decline and reduces senile plaque burden in APP/PS1$^{+/-}$ mice. (**A**) Timeline (in days) for levamisole treatment and Open Field (OF), Elevated Plus Maze (EPM), T-maze (TM) and Barnes Maze Test (BT or t-BT for training) behavioral assays performed by WT ($n=12$ or 10), WT treated with levamisole (WT/Leva, $n=6$), APP/PS1$^{+/-}$ untreated ($n=12$ or 10) and treated with levamisole (APP/PS1$^{+/-}$/Leva, $n=6$–8) groups. When indicated, black square data points represent males and open square data points represent females. (**B**) TNAP activity in hippocampal homogenates (left graph) and plasma (right graph) from WT ($n=12$), WT/Leva ($n=6$), none-treated APP/PS1$^{+/-}$ ($n=12$), and APP/PS1$^{+/-}$/Leva ($n=7$) mice. Data are given as a percentage relative to WT mice, and graphs show the distribution of values per group (median, IQR, maximum, and minimum values). (**C**) Percentage of time in open arms in the EPM. (**D**) Latency to escape hole across the training sessions of the Barnes test. (**E**) Time spent (left graph) and distance traveled (right graph) to find the escape hole in BT in test day. (**F**) Percentage of time in the new arm during the TM. * $P \leq 0.05$ or ** $P \leq 0.01$; using a one-way ANOVA followed by Tukey's post hoc test. (**G**) Representative confocal microscopy image of senile plaques (Aβ, red channel) in the hippocampus of APP/PS1$^{+/-}$/Leva mice. Nuclei were stained with DAPI. Scale bar: 500 µm. (**H**, **I**) Graphs represent the distribution of values per group (median, IQR, maximum, and minimum values) of the percentage of area (**H**) and number (**I**) of hippocampal senile plaques. ** $P \leq 0.01$; using an unpaired two-tailed Student's *t*-test. **J**. Representative immunofluorescence image of hippocampal sections stained with the microglial marker Iba-1 (green channel) used to assess microglial density in the vicinity of senile plaques (Aβ, red channel) in APP/PS1$^{+/-}$/Leva mice. Distances of 40 and 80 µm from the periphery of senile plaques are identified with white dashed lines. Scale bar: 50 µm. (**K**, **L**) The graphs represent the distribution of values per group (median, IQR, maximum, and minimum values) of the density of hippocampal microglia per plaque area (µm^2) (**K**) and the percentage of microglia cells found in every delimitated area (**L**) (n ≧ five mice per genotype). ** $P \leq 0.01$; using an unpaired two-tailed Student's *t*-test or *** $P \leq 0.001$; using a one-way ANOVA followed by Tukey's post hoc test. (**M**) Representative single confocal microscopy plane and orthogonal views showing CD68 positive-phagocytic microvesicles (red channel) phagocytosing Aβ peptides (Aβ, grey channel) within microglia (Iba-1, green channel) surrounding hippocampal senile plaques in APP/PS1$^{+/-}$/Leva mice. (**N**) Graph represents the percentage of lysosomes containing amyloid-β of the total microglial lysosomes. * $P \leq 0.05$, using an unpaired two-tailed Student's *t*-test. Data in box plots represent the distribution of values per group (median, IQR, maximum, and minimum values)

primary somatosensory cortex and the lateral and medial parietal association cortex from a sub-cohort of APP/PS1$^{+/-}$ and levamisole-treated APP/PS1$^{+/-}$ mice (supplementary Fig. 3 C-E). Again, non-significant sex-related differences were found (Fig. 4H-I). Further analysis confirmed that this decrease was not caused by a reduction in the amyloidogenic processing of the APP protein or by a decrease in its levels (Supplementary Fig. 3F-J). Interestingly, as observed by partial *Akp2* gene silencing, pharmacological inhibition of TNAP caused an increase recruitment of microglial cells toward senile plaques, promoting a rise in the microglial density inside the plaques (Fig. 4J-L), and increased phagocytic Aβ capacity of microglia in APP/PS1$^{+/-}$ mice (Fig. 4M and N). Of note, these changes were accompanied by a significant increase in the cleaved OPN levels (Fig. 5A-B) or total OPN protein levels (Fig. 5A and C), as well as mRNA levels of this protein (Supplementary Fig. 3K).

Regarding neuroinflammation, although levamisole treatment avoided the increased P2X7R levels in APP/PS1$^{+/-}$ mice (both at the protein and messenger levels, Fig. 5D-E and Supplementary Fig. 3L), it did not prevent the rise levels of interleukin 1 beta (IL1β) nor NOD-like receptor family pyrin domain containing 3 (NLRP3) detected in these mice (Fig. 5D, F-G and Supplementary Fig. 3M and 3 N).

Finally, consistent with the genetic approach´s results, pharmacological inhibition of TNAP prevented the decrease in hippocampal LRP1 levels (Fig. 5D and H) and increased the serum human $A\beta_{1-40}$ levels in APP/PS1$^{+/-}$ mice (Fig. 5I). Nevertheless, pharmacological TNAP inhibition failed to prevent the reduction of metalloprotease MMP9 levels (Fig. 5D and J).

Discussion

In the present study, we report for the first time that genetic or pharmacological TNAP blockage in a mouse model of FAD promotes the clearance of cerebral senile plaques and rescues the cognitive decline caused by Aβ-induced toxicity. These beneficial effects are due to the fact that TNAP blockade (i) promotes the microglial recruitment toward senile plaque (ii) increases microglial capacity to phagocytose Aβ, (iii) favors the LRP1-mediated Aβ transport at the BBB, and (iv) promotes expression of MMP9, a metalloprotease involved in both senile plaque degradation and in the OPN processing, a substrate of TNAP that regulates phagocytic and recruitment microglial properties.

Perhaps one of the most unexpected results reported here is the fact that TNAP inhibition promotes the microglial Aβ phagocytosis. This is mainly due to previous works failing to detect TNAP activity in microglial cells from rodents' brains under physiological conditions [49]. In contrast, here we found that microglial cells present an unusually scattered punctuated labeling for TNAP in APP/PS1$^{+/-}$ mice, a mouse model of amyloidosis, which is also observed inside senile plaques. Remarkably, a similar TNAP expression pattern was observed inside senile plaques of AD patients. But why do microglial cells express TNAP when they are recruited inside senile plaques? Growing evidence might suggest that microglial TNAP may have an anti-inflammatory role. Thus, it was reported that TNAP contributes to the dephosphorylation of Toll-like receptor ligands like LPS, mitigating inflammasome activation and cytokines secretion [50]. Also, TNAP dephosphorylates, among others, extracellular nucleotides yield adenosine as the final product, playing, in this way, a critical role in balancing pro-inflammatory ATP and anti-inflammatory adenosine [51]. In the same line, it was described that LPS-induced

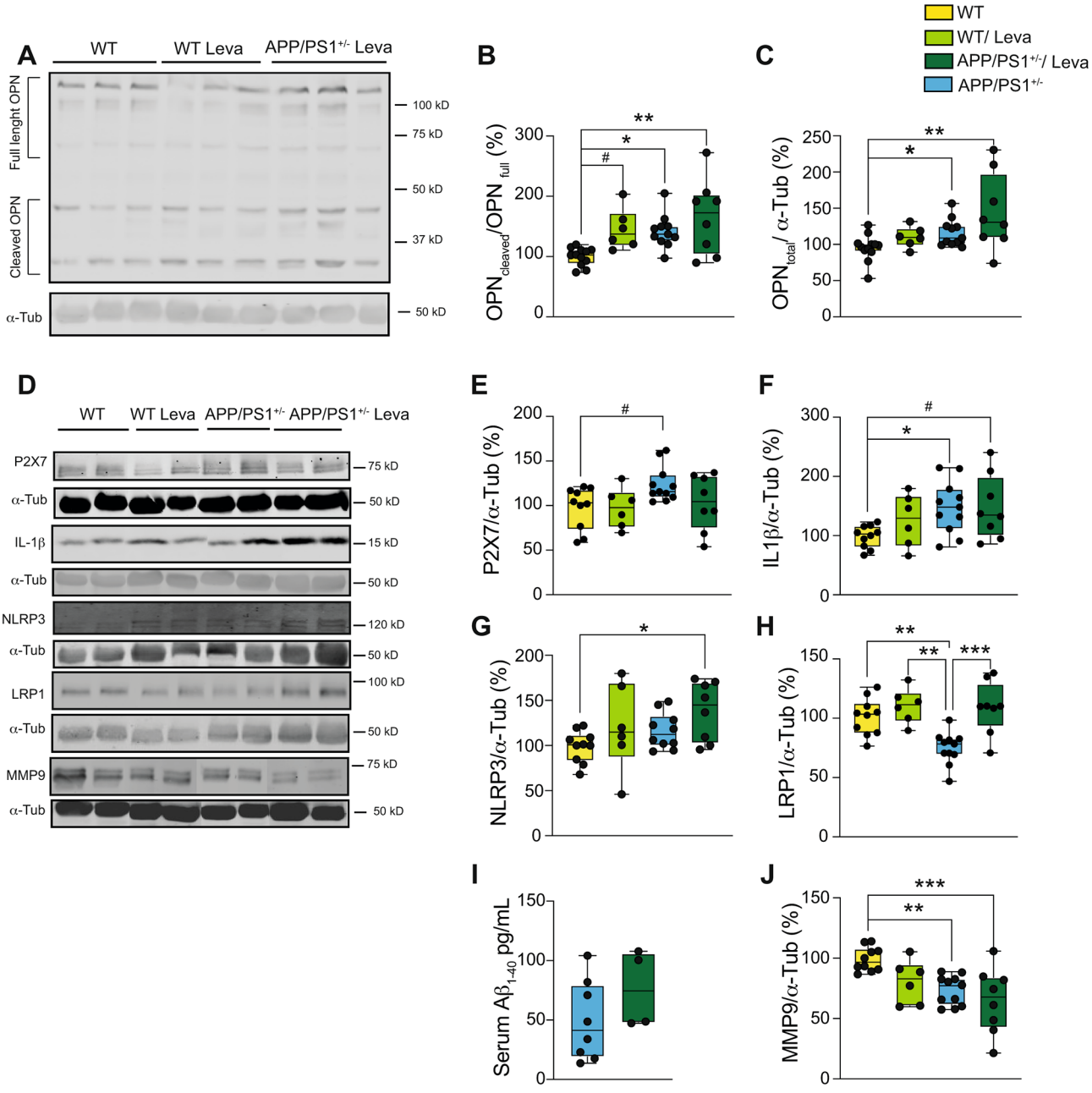

Fig. 5 TNAP pharmacological inhibition leads to increased levels of OPN, P2X7, and LRP1 in APP/PS1$^{+/-}$mice. (**A**) Representative immunoblot using an antibody recognizing cleaved and full-length OPN in homogenates from the hippocampus of WT, WT treated with Levamisole (WT Leva), APP/PS1$^{+/-}$, and APP/PS1$^{+/-}$ treated with Levamisole (APP/PS1$^{+/-}$ Leva). (**B** and **C**) Quantification of the ratio between cleaved OPN and full-length OPN (**K**) and total OPN (**L**) protein levels in the hippocampus of WT ($n=12$), WT Leva ($n=6$), APP/PS1$^{+/-}$ Leva ($n=8$) and APP/PS1$^{+/-}$ ($n=11$) mice. (**D**) Representative immunoblot of LRP1, IL-1β, P2X7, NLRP3, and MMP9 in homogenates from the hippocampus of WT, Levamisole-treated WT (WT Leva), untreated APP/PS1$^{+/-}$, and Levamisole-treated APP/PS1$^{+/-}$ (APP/PS1$^{+/-}$ Leva) mice. Quantification of P2X7 (**E**), IL-1β (**F**), NLRP3 (**G**), LRP1 (**H**), and MMP9 (**J**) protein levels in the hippocampus of WT ($n=10$), WT Leva ($n=6$), APP/PS1$^{+/-}$ Leva ($n=8$) and APP/PS1$^{+/-}$ ($n=11$) mice. Levels of α-tubulin were used as loading control for normalization purposes. Data are given as a percentage relative to WT mice $^{\#}P \leq 0{,}08$, * $P \leq 0.05$ or ** $P \leq 0.01$, using a one-way ANOVA followed by Tukey's post hoc test. **I**. Graphs show the $A\beta_{1-40}$ levels in serum samples from APP/PS1$^{+/-}$ ($n=8$), the same that were previously shown in Fig. 3O, and APP/PS1$^{+/-}$ Leva ($n=4$) mice. Serum samples were analyzed via $A\beta_{1-40}$-detecting ELISA. Data in box plots represent the distribution of values per group (median, IQR, maximum, and minimum values)

neuroinflammation causes hippocampal TNAP expression upregulation [20], and TNAP inhibition increases the IL1β secretion [51], probably by exacerbating ATP-associated NLPR3 activation [52]. Interestingly, TNAP inhibition also leads to pyrophosphate (PPi) accumulation, initiating the formation of calcium pyrophosphate dihydrate crystals [53], which in turn can induce NLRP3 inflammasome activation [54]. However, a local increase of PPi also causes upregulation of OPN [55], a glycoprotein that promotes neuroprotective effects in various brain diseases [41, 56]. Those findings suggest that TNAP plays a more complex role in microglial functionality. Indeed, a recent study has reported that upregulation of OPN, especially its fragments cleaved by metalloproteases, increases the clearance of Aβ by blood-derived microglia, specifically by monocyte-derived macrophages, and promotes their anti-inflammatory phenotype in a mouse model of AD [35]. In agreement with previous studies reporting that *Akp2* depletion promotes OPN expression [57], we found that TNAP deficiency increases the OPN messenger levels, but, in addition, induces a greater proportion of anti-inflammatory OPN C-terminals fragments MMP-cleaved than WT or APP/PS1$^{+/-}$ mice. Accompanying these results, we also found that TNAP deficiency reverts the downregulation of MMP9 in APP/PS1$^{+/-}$ mice. Therefore, our findings strongly suggest that the increased phagocytic capacity of microglia observed in APP/PS1$^{+/-}$/TNAP$^{+/-}$ mice, and hence the reduction in brain senile plaque burden, can be attributed to the increased generation of OPN C-terminal fragments cleaved by MMP9. Besides, because OPN is a TNAP-substrate [23], and previous work reported that phosphorylation of the OPN N-terminal domain promotes cell migration and subsequent activation by engagement of β3 integrin receptors [58], we postulated that genetic or pharmacological TNAP inhibition promotes OPN phosphorylation, which improves microglial migration capacity, thereby contributing to a more efficient reduction in senile plaque burden. Interestingly, it was also reported that the phosphorylated *N* terminal fragment of OPN induces a strong response of MMP9 [58]. However, because in APP/PS1 mice changes in cleaved OPN forms observed were matched with a reduction in MMP9 expression, the involvement of other proteases in OPN processing in ASPP/PS1 mice was evidenced. Indeed, other metalloproteases have also been related to posttranslational OPN processing [24]. Therefore, additional studies should be conducted further to understand the effects of TNAP in OPN-processing proteases and determine its involvement in the beneficial effect observed here. Furthermore, in accordance with previous work reporting that administration of recombinant OPN downregulates NLRP3 expression and reduces the IL-1β release in a mouse model of LPS-induced inflammation [59], here we find TNAP haploinsufficiency prevents increased expression of inflammasome members NLRP3 and P2X7R in APP/PS1$^{+/-}$ mice, although it fails to reduce the IL-1β release. This unexpected result may be due to the fact that TNAP inhibition also reduces extracellular ATP degradation, and thus favors ATP-associated NLRP3 activation [52]. However, further studies are needed to clarify this point, including a more detailed analysis of the cytokine profile induced by pharmacological or genetic blockade of TNAP in the brain. Supporting the relevance to control de axis NLRP3/P2X7R/IL1β as a putative therapeutic strategy to treat AD, it has recently been reported that blocking inflammasome activation by NLRP3 knockdown enhances phagocytic capacity to clear Aβ preventing the spatial memory loss in APP/PS1$^{+/-}$ mice [60].

Given that reduced Aβ load might be due to increased Aβ transport through the BBB [12], we elucidate whether induced TNAP deficiency affects LRP1 functionality, a factor promoting Aβ transport in abluminal-to-luminal (brain-to-blood) transport of Aβ [45]. Relevance of LRP1 in Aβ transport from the brain to blood was evidenced by the finding that selective LRP1 antibodies against LRP1 substantially inhibit $A\beta_{1-40}$ transport at BBB [44], or by observing that selective LRP1 depletion in vascular smooth muscle cells increases cerebral Aβ deposition in APP/PS1$^{+/-}$ mice [61]. In accordance with previous work [46], we found that APP/PS1$^{+/-}$ mice have reduced expression of LRP1 in the hippocampus, which is prevented when TNAP is present in hemizygosity. Moreover, we found that both APP/PS1$^{+/-}$/TNAP$^{+/-}$ and levamisole-treated APP/PS1$^{+/-}$ mice present higher $A\beta_{1-40}$ serum levels than APP/PS1$^{+/-}$ mice. In light of these findings, we can conclude that TNAP also promotes the $A\beta_{1-40}$ transport across BBB.

Finally, our results suggest that pharmacological TNAP inhibition may be considered a potential therapeutic strategy to effectively reduce the Aβ burden associated with AD since. This claim is supported by the fact that, similarly to genetic TNAP disruption, levamisole treatment, a widely used BBB-permeable TNAP inhibitor, reduced cerebral plaque burden by increasing the phagocytosis of Aβ and its transport throughout the BBB. Nevertheless, levamisole treatment did not reproduce the reduction in the size of senile plaques observed in APP/PS1$^{+/-}$/TNAP$^{+/-}$ mice. Given that MMP9 can degrade amyloid-β-fibrils from compact plaques in APP/PS1$^{+/-}$ mice [48], the inability of levamisole to prevent the reduced MMP9 expression in APP/PS1$^{+/-}$ mice might underlie this unexpected result. But why did levamisole treatment fail to prevent some beneficial effects observed in APP/PS1$^{+/-}$/TNAP$^{+/-}$ mice, such as avoiding the increased NLRP3 or reducing MMP9 expression levels? The reason is unknown, but it is important to note that

levamisole, in addition to effectively blocking TNAP, also has off-target effects on the brain [62]. Supporting this hypothesis, only very limited beneficial effects were observed in the levamisole-treated APP/PS1$^{+/-}$ mice in behavioral tests. For this reason, additional efforts should be made to develop selective and BBB-permeable TNAP antagonists.

Conclusions

Our results, provide for the first time that brain blockade of TNAP efficiently reduces the Aβ load in an amyloid mouse model and, consequently, ameliorates the behavioral alterations associated with Aβ-induced toxicity. These beneficial effects are due to the fact that TNAP-blockade promotes the generation of MMP-cleaved OPN C-terminal fragments cleaved by MMP and OPN phosphorylation, which in turn promotes the blood-derived microglia recruitment toward the senile plaque and increases their capacity to phagocytose Aβ. Besides, the TNAP blockade also favors the LRP1-mediated Aβ transport at the BBB, which also contributes to reducing brain Aβ burden. Considering that previous findings from our group have provided solid evidence supporting that TNAP blockade also ameliorates Tau-induced neurotoxicity and increases life expectancy in a mouse model mimicking tau pathology associated with AD, we can claim that TNAP blockade may be a novel and effective therapy for the treatment of AD patients.

Abbreviations

AD	Alzheimer's disease
Aβ	Amyloid-b peptide
TNAP	Tissue non-specific alkaline phosphatase
APP	Amyloid precursor protein
PS1 and PS2	Presenilin-1 and – 2
FAD	Early-onset familial AD
MCI	Middle cognitive impairment
OPN	Osteopontin
P2X7R	P2X7 receptor
UCM	Universidad Complutense de Madrid
WT	Wild-type
BBB	Blood-brain barrier
PBS	Phosphate-buffered saline
RT	Room temperature
Dapi	4',6-diamidino-2-phenylindole
OF	Open field test
EPM	Elevated plus maze test
LRP1	Low-density lipoprotein receptor-related protein 1
MMP9	Metalloproteinase-9
IL1β	Interleukin 1 beta
NLRP3	NOD-like receptor family pyrin domain containing 3
LPS	Lipopolysaccharide
BSA	Bovine serum albumin
PPi	Pyrophosphate

Supplementary Information

The online version contains supplementary material available at https://doi.org/10.1186/s13195-024-01600-x.

Supplementary Material 1

Supplementary Material 2

Author contributions

L.S-T processed the transgenic mice, generated and analyzed the samples, participated in experimental design, and contributed to the interpretation of the data; L.R bred and processed the transgenic mice, generated and analyzed the samples; A. S-S generated and analyzed the samples, participated in experimental design, contributed to the interpretation of the data and revised the manuscript; P.A. generated and analyzed the samples, participated in experimental design, and revised the manuscript; B.A-C contributed to the interpretation of the result and revised the manuscript; M.D-H participated in mouse breeding and processing, generated and analyzed the samples, participated in the experimental design, contributed to the interpretation of the results, wrote the manuscript and provided financial support for the work. All authors read and approved the final manuscript.

Funding

This work was supported by funding from the following: Spanish Ministry of Economy and Competitiveness RTI2018-095753-B-I00 and PID2021-125364OB-I00 (to M.D.-H.); European Union project H2020-MSCA-ITN-2017 number 766124 (to M.D.-H.); and UCM-Santander Central Hispano BankPR41/17-21014 (to M.D.-H.). A. S-S is recipient of a Ramon y Cajal contract, reference RYC2022-035922-I, funded by MCIN/AEI/https://doi.org/10.13039/501100011033 and Fondo Social Europeo Plus (FSE+).

Data availability

No datasets were generated or analysed during the current study.

Declarations

Ethics approval and consent to participate

For human samples. A written informed consent for brain removal after death for diagnostic and research purposes was obtained from the brain donors and/or next of kin. Procedures, information, and consent forms were approved by the Bioethics Subcommittee of Fundación Cien Madrid, Spain (S19001). All animal procedures were carried out at the Universidad Complutense de Madrid (UCM) in compliance with National and European regulations (RD1201/2005; 86/609/CEE) and following the International Council for the Laboratory Animal Science guidelines. The protocol for animal experiments was approved by the Committee of Animal Experiments at the UCM and the Environmental Counselling of the Comunidad de Madrid, Spain (PROEX 137.8/22).

Consent for publication

Not applicable.

Competing interests

The authors declare no competing interests.

Author details

[1]Department of Biochemistry and Molecular Biology, Veterinary School, Complutense University of Madrid, Avda. Puerta de Hierro S/N, Madrid 28040, Spain
[2]Instituto de Investigación Sanitaria del Hospital Clínico San Carlos, IdISSC, Madrid, Spain
[3]Department of Biochemistry and Molecular Biology, Medical School, Complutense University of Madrid, Plaza Ramón y Cajal, S/N, Madrid 28040, Spain

Received: 24 July 2024 / Accepted: 9 October 2024
Published online: 22 October 2024

References

1. Lee VM, Goedert M, Trojanowski JQ. Neurodegenerative tauopathies. Annu Rev Neurosci. 2001;24:1121–59.
2. Selkoe DJ. Alzheimer's disease: genes, proteins, and therapy. Physiol Rev. 2001;81(2):741–66.

3. Ling Y, Morgan K, Kalsheker N. Amyloid precursor protein (APP) and the biology of proteolytic processing: relevance to Alzheimer's disease. Int J Biochem Cell Biol. 2003;35(11):1505–35.
4. Price DL, Sisodia SS. Mutant genes in familial Alzheimer's disease and transgenic models. Annu Rev Neurosci. 1998;21:479–505.
5. Palmqvist S, Scholl M, Strandberg O, Mattsson N, Stomrud E, Zetterberg H, et al. Earliest accumulation of beta-amyloid occurs within the default-mode network and concurrently affects brain connectivity. Nat Commun. 2017;8(1):1214.
6. Sperling R, Mormino E, Johnson K. The evolution of preclinical Alzheimer's disease: implications for prevention trials. Neuron. 2014;84(3):608–22.
7. Maia MA, Sousa E. BACE-1 and gamma-Secretase as Therapeutic Targets for Alzheimer's Disease. Pharmaceuticals (Basel). 2019;12(1).
8. Zhao Z, Pissarnitski DA, Huang X, Palani A, Zhu Z, Greenlee WJ, et al. Discovery of a Tetrahydrobenzisoxazole Series of gamma-secretase modulators. ACS Med Chem Lett. 2017;8(10):1002–6.
9. Rafii MS, Skotko BG, McDonough ME, Pulsifer M, Evans C, Doran E, et al. A Randomized, Double-Blind, Placebo-Controlled, phase II study of oral ELND005 (scyllo-Inositol) in young adults with Down Syndrome without Dementia. J Alzheimers Dis. 2017;58(2):401–11.
10. Tsiknia AA, Sundermann EE, Reas ET, Edland SD, Brewer JB, Galasko D, et al. Sex differences in Alzheimer's disease: plasma MMP-9 and markers of disease severity. Alzheimers Res Ther. 2022;14(1):160.
11. Seok H, Lee M, Shin E, Yun MR, Lee YH, Moon JH, et al. Low-dose pioglitazone can ameliorate learning and memory impairment in a mouse model of dementia by increasing LRP1 expression in the hippocampus. Sci Rep. 2019;9(1):4414.
12. Vaz M, Silvestre S. Alzheimer's disease: recent treatment strategies. Eur J Pharmacol. 2020;887:173554.
13. Self WK, Holtzman DM. Emerging diagnostics and therapeutics for Alzheimer disease. Nat Med. 2023;29(9):2187–99.
14. Kang C. Donanemab: First Approval. Drugs. 2024.
15. Sevigny J, Chiao P, Bussiere T, Weinreb PH, Williams L, Maier M, et al. The antibody aducanumab reduces Abeta plaques in Alzheimer's disease. Nature. 2016;537(7618):50–6.
16. van Dyck CH, Swanson CJ, Aisen P, Bateman RJ, Chen C, Gee M, et al. Lecanemab in Early Alzheimer's Disease. N Engl J Med. 2023;388(1):9–21.
17. Cummings J, Apostolova L, Rabinovici GD, Atri A, Aisen P, Greenberg S, et al. Lecanemab: appropriate use recommendations. J Prev Alzheimers Dis. 2023;10(3):362–77.
18. Vaz M, Silva V, Monteiro C, Silvestre S. Role of Aducanumab in the treatment of Alzheimer's Disease: challenges and opportunities. Clin Interv Aging. 2022;17:797–810.
19. Vardy ER, Kellett KA, Cocklin SL, Hooper NM. Alkaline phosphatase is increased in both brain and plasma in Alzheimer's disease. Neurodegener Dis. 2012;9(1):31–7.
20. Sebastian-Serrano A, Merchan-Rubira J, Di Lauro C, Bianchi C, Soria-Tobar L, Narisawa S, et al. TNAP upregulation is a critical factor in Tauopathies and its blockade ameliorates neurotoxicity and increases life-expectancy. Neurobiol Dis. 2022;165:105632.
21. Aivar P, Bianchi C, Di Lauro C, Soria-Tobar L, Alvarez-Castelao B, Calero M et al. TNAP and P2X7R: New Plasma Biomarkers for Alzheimer's Disease. Int J Mol Sci. 2023;24(13).
22. Diaz-Hernandez M, Gomez-Ramos A, Rubio A, Gomez-Villafuertes R, Naranjo JR, Miras-Portugal MT, et al. Tissue-nonspecific alkaline phosphatase promotes the neurotoxicity effect of extracellular tau. J Biol Chem. 2010;285(42):32539–48.
23. Narisawa S, Yadav MC, Millan JL. In vivo overexpression of tissue-nonspecific alkaline phosphatase increases skeletal mineralization and affects the phosphorylation status of osteopontin. J Bone Min Res. 2013;28(7):1587–98.
24. Lalwani RC, Volmar CH, Wahlestedt C, Webster KA, Shehadeh LA. Contextualizing the Role of Osteopontin in the Inflammatory Responses of Alzheimer's Disease. Biomedicines. 2023;11(12).
25. Diez-Zaera M, Diaz-Hernandez JI, Hernandez-Alvarez E, Zimmermann H, Diaz-Hernandez M, Miras-Portugal MT. Tissue-nonspecific alkaline phosphatase promotes axonal growth of hippocampal neurons. Mol Biol Cell. 2011;22(7):1014–24.
26. Diaz-Hernandez JI, Gomez-Villafuertes R, Leon-Otegui M, Hontecillas-Prieto L, Del Puerto A, Trejo JL, et al. In vivo P2X7 inhibition reduces amyloid plaques in Alzheimer's disease through GSK3beta and secretases. Neurobiol Aging. 2012;33(8):1816–28.
27. Chen X, Hu J, Jiang L, Xu S, Zheng B, Wang C, et al. Brilliant blue G improves cognition in an animal model of Alzheimer's disease and inhibits amyloid-beta-induced loss of filopodia and dendrite spines in hippocampal neurons. Neuroscience. 2014;279:94–101.
28. Martin E, Amar M, Dalle C, Youssef I, Boucher C, Le Duigou C, et al. New role of P2X7 receptor in an Alzheimer's disease mouse model. Mol Psychiatry. 2019;24(1):108–25.
29. Jankowsky JL, Slunt HH, Ratovitski T, Jenkins NA, Copeland NG, Borchelt DR. Co-expression of multiple transgenes in mouse CNS: a comparison of strategies. Biomol Eng. 2001;17(6):157–65.
30. Narisawa S, Frohlander N, Millan JL. Inactivation of two mouse alkaline phosphatase genes and establishment of a model of infantile hypophosphatasia. Dev Dyn. 1997;208(3):432–46.
31. Fernandez M, Garcia JJ, Sierra M, Diez MJ, Teran MT. Bioavailability of levamisole after intramuscular and oral administration in sheep. N Z Vet J. 1998;46(5):173–6.
32. Attar A, Liu T, Chan WT, Hayes J, Nejad M, Lei K, et al. A shortened Barnes maze protocol reveals memory deficits at 4-months of age in the triple-transgenic mouse model of Alzheimer's disease. PLoS ONE. 2013;8(11):e80355.
33. Paxinos G KF, editor. Mouse brain in stereotaxic coordinates, Compact. New York Academic; 2008.
34. Martinez-Frailes C, Di Lauro C, Bianchi C, de Diego-Garcia L, Sebastian-Serrano A, Bosca L, et al. Amyloid Peptide Induced Neuroinflammation Increases the P2X7 Receptor Expression in Microglial Cells, Impacting on Its Functionality. Front Cell Neurosci. 2019;13:143.
35. Rentsendorj A, Sheyn J, Fuchs DT, Daley D, Salumbides BC, Schubloom HE, et al. A novel role for osteopontin in macrophage-mediated amyloid-beta clearance in Alzheimer's models. Brain Behav Immun. 2018;67:163–80.
36. Hulshof LA, Frajmund LA, van Nuijs D, van der Heijden DCN, Middeldorp J, Hol EM. Both male and female APPswe/PSEN1dE9 mice are impaired in spatial memory and cognitive flexibility at 9 months of age. Neurobiol Aging. 2022;113:28–38.
37. Reiserer RS, Harrison FE, Syverud DC, McDonald MP. Impaired spatial learning in the APPSwe + PSEN1DeltaE9 bigenic mouse model of Alzheimer's disease. Genes Brain Behav. 2007;6(1):54–65.
38. Zhang W, Hao J, Liu R, Zhang Z, Lei G, Su C, et al. Soluble abeta levels correlate with cognitive deficits in the 12-month-old APPswe/PS1dE9 mouse model of Alzheimer's disease. Behav Brain Res. 2011;222(2):342–50.
39. Locci A, Orellana H, Rodriguez G, Gottliebson M, McClarty B, Dominguez S, et al. Comparison of memory, affective behavior, and neuropathology in APP(NLGF) knock-in mice to 5xFAD and APP/PS1 mice. Behav Brain Res. 2021;404:113192.
40. Prinz M, Priller J, Sisodia SS, Ransohoff RM. Heterogeneity of CNS myeloid cells and their roles in neurodegeneration. Nat Neurosci. 2011;14(10):1227–35.
41. Chan JL, Reeves TM, Phillips LL. Osteopontin expression in acute immune response mediates hippocampal synaptogenesis and adaptive outcome following cortical brain injury. Exp Neurol. 2014;261:757–71.
42. Kaartinen MT, Pirhonen A, Linnala-Kankkunen A, Maenpaa PH. Transglutaminase-catalyzed cross-linking of osteopontin is inhibited by osteocalcin. J Biol Chem. 1997;272(36):22736–41.
43. Scatena M, Liaw L, Giachelli CM. Osteopontin: a multifunctional molecule regulating chronic inflammation and vascular disease. Arterioscler Thromb Vasc Biol. 2007;27(11):2302–9.
44. Shibata M, Yamada S, Kumar SR, Calero M, Bading J, Frangione B, et al. Clearance of Alzheimer's amyloid-ss(1–40) peptide from brain by LDL receptor-related protein-1 at the blood-brain barrier. J Clin Invest. 2000;106(12):1489–99.
45. Shinohara M, Tachibana M, Kanekiyo T, Bu G. Role of LRP1 in the pathogenesis of Alzheimer's disease: evidence from clinical and preclinical studies. J Lipid Res. 2017;58(7):1267–81.
46. He Y, Ruganzu JB, Zheng Q, Wu X, Jin H, Peng X, et al. Silencing of LRP1 exacerbates Inflammatory Response Via TLR4/NF-kappaB/MAPKs signaling pathways in APP/PS1 transgenic mice. Mol Neurobiol. 2020;57(9):3727–43.
47. Deane R, Wu Z, Sagare A, Davis J, Du Yan S, Hamm K, et al. LRP/amyloid beta-peptide interaction mediates differential brain efflux of Abeta isoforms. Neuron. 2004;43(3):333–44.
48. Yan P, Hu X, Song H, Yin K, Bateman RJ, Cirrito JR, et al. Matrix metalloproteinase-9 degrades amyloid-beta fibrils in vitro and compact plaques in situ. J Biol Chem. 2006;281(34):24566–74.
49. Langer D, Hammer K, Koszalka P, Schrader J, Robson S, Zimmermann H. Distribution of ectonucleotidases in the rodent brain revisited. Cell Tissue Res. 2008;334(2):199–217.

50. Pettengill M, Matute JD, Tresenriter M, Hibbert J, Burgner D, Richmond P, et al. Human alkaline phosphatase dephosphorylates microbial products and is elevated in preterm neonates with a history of late-onset sepsis. PLoS ONE. 2017;12(4):e0175936.
51. Bessueille L, Briolay A, Como J, Mebarek S, Mansouri C, Gleizes M, et al. Tissue-nonspecific alkaline phosphatase is an anti-inflammatory nucleotidase. Bone. 2020;133:115262.
52. Karmakar M, Katsnelson MA, Dubyak GR, Pearlman E. Neutrophil P2X7 receptors mediate NLRP3 inflammasome-dependent IL-1beta secretion in response to ATP. Nat Commun. 2016;7:10555.
53. Beck C, Morbach H, Richl P, Stenzel M, Girschick HJ. How can calcium pyrophosphate crystals induce inflammation in hypophosphatasia or chronic inflammatory joint diseases? Rheumatol Int. 2009;29(3):229–38.
54. Martinon F, Petrilli V, Mayor A, Tardivel A, Tschopp J. Gout-associated uric acid crystals activate the NALP3 inflammasome. Nature. 2006;440(7081):237–41.
55. Harmey D, Hessle L, Narisawa S, Johnson KA, Terkeltaub R, Millan JL. Concerted regulation of inorganic pyrophosphate and osteopontin by akp2, enpp1, and ank: an integrated model of the pathogenesis of mineralization disorders. Am J Pathol. 2004;164(4):1199–209.
56. Brown A, Osteopontin. A key link between immunity, inflammation and the Central Nervous System. Transl Neurosci. 2012;3(3):288–93.
57. Harmey D, Johnson KA, Zelken J, Camacho NP, Hoylaerts MF, Noda M, et al. Elevated skeletal osteopontin levels contribute to the hypophosphatasia phenotype in Akp2(-/-) mice. J Bone Min Res. 2006;21(9):1377–86.
58. Weber GF, Zawaideh S, Hikita S, Kumar VA, Cantor H, Ashkar S. Phosphorylation-dependent interaction of osteopontin with its receptors regulates macrophage migration and activation. J Leukoc Biol. 2002;72(4):752–61.
59. Zhang X, Shu Q, Liu Z, Gao C, Wang Z, Xing Z, et al. Recombinant osteopontin provides protection for cerebral infarction by inhibiting the NLRP3 inflammasome in microglia. Brain Res. 2021;1751:147170.
60. Heneka MT, Kummer MP, Stutz A, Delekate A, Schwartz S, Vieira-Saecker A, et al. NLRP3 is activated in Alzheimer's disease and contributes to pathology in APP/PS1 mice. Nature. 2013;493(7434):674–8.
61. Kanekiyo T, Liu CC, Shinohara M, Li J, Bu G. LRP1 in brain vascular smooth muscle cells mediates local clearance of Alzheimer's amyloid-beta. J Neurosci. 2012;32(46):16458–65.
62. Nowak LG, Rosay B, Czege D, Fonta C. Tetramisole and Levamisole suppress neuronal activity independently from their inhibitory action on tissue non-specific alkaline phosphatase in mouse cortex. Subcell Biochem. 2015;76:239–81.

Publisher's note